Supporting Information

Toward highly efficient TADF-active Cu(I), Ag(I) and Au(I) carbene complexes using symmetry-based design strategy

Alexander V. Artem'ev,*[a] Maxim I. Rogovoy,[a] Ilia M. Odud,[b,c] Maria P. Davydova,[a] Marianna I. Rakhmanova,[a] Pavel A. Petrov,[a] Valery K. Brel,[d] Oleg I. Artushin,[d] Konstantin A. Brylev,[a] Denis G. Samsonenko,[a] Alexey S. Berezin,[a] Dmitry E. Gorbunov,[b] Nina P. Gritsan[b]*

[a] *Nikolaev Institute of Inorganic Chemistry, SB RAS, 3, Lavrentiev Ave., 630090 Novosibirsk, Russia*
[b] *Voevodsky Institute of Chemical Kinetics and Combustion, SB RAS, 3, Institutskaya Str., 630090 Novosibirsk, Russia*
[c] *Novosibirsk State University, 1, Pirogova Str. 630090 Novosibirsk, Russia*
[d] *Nesmeyanov Institute of Element Organic Compounds, RAS, Moscow, Russia*

*E-mail: chemisufarm@yandex.ru (Alexander V. Artem'ev), gritsan@kinetics.nsc.ru (Nina P. Gritsan)

Table of contents

§1. Reagents and instrumentation details

1,2,4,5-Tetrakis(diphenylphosphino)benzene[1] and carbene precursors[2–5] were synthesized according to the known procedures. Sodium tetraphenylborate (≥99.5%, Sigma-Aldrich) was used as purchased. All the solvents were purified prior to use by common methods.

The CHN microanalyses were performed on a MICRO cube analyzer.

Thermogravimetric analyses were carried out in a closed Al_2O_3 pan under argon flow at 10 °C/min heating rate using a Netzsch STA 449 F1 Jupiter STA.

***mid*-IR spectra** were recorded on a Bruker Vertex 80 FT-spectrometer in KBr pellets at ambient temperature.

Excitation and emission spectra were recorded on a Fluorolog 3 spectrometer (Horiba Jobin Yvon) with a cooled PC177CE-010 photon detection module equipped with an R2658 photomultiplier. The emission decays were recorded on the same instrument. The absolute PLQYs were measured at 298 K using a Fluorolog 3 Quanta-phi integrating sphere. The temperature dependences of the spectra and luminescence lifetimes were recorded using Optistat DN optical cryostats (Oxford Instruments).

UV-Vis absorption spectra in CH_2Cl_2 solutions were recorded on a Shimadzu UV-3101 spectrophotometer at 200–800 nm (10^{-5} mol·L^{-1}, 298 K).

NMR spectra were registered using a Bruker AV-500 spectrometer at 500 (^{1}H), 126 (^{13}C) and 202 (^{31}P) MHz, with solvent peaks as reference, at room temperature. The ^{31}P{^{1}H} NMR shifts are referenced respective to 85% H_3PO_4/D_2O as an external standard.

Solid state reflectance spectra were also recorded on a Shimadzu UV-3101 spectrophotometer. Samples were prepared by a thorough grinding of a mixture of a complex (~0.05 mol%) with $BaSO_4$. The reflectance data were further converted into a Kubelka-Munk function (K-M function, $\frac{K}{S}$)[6] using $BaSO_4$ as a standard (100% reflectance). In the case of a low content of the complex in the mixture (< 1 mol%), this function is proportional to the absorption coefficient K of the compound under study and inversely proportional to the scattering coefficient S of the standard ($BaSO_4$).

$$\frac{K}{S} = \frac{(1 - R_\infty)^2}{2R_\infty},$$

where R_∞ is the reflectance for a sufficiently large layer thickness. Under these conditions, the Kubelka-Munk function is linear in the concentration of the investigated substance.

§2. Synthetic procedures

Complex [Cu$_2$(IPr)$_2$(μ_4-tpbz)](BPh$_4$)$_2$·0.4Me$_2$CO (**1**·0.4Me$_2$CO)

To a mixture of [Cu(IPr)Cl] (29.5 mg, 0.061 mmol), 1,2,4,5-tetrakis(diphenylphosphino)benzene (25.2 mg, 0.031 mmol) and NaBPh$_4$ (20.9 mg, 0.061 mmol), acetone (2 mL) was added and a suspension was stirred at ambient temperature for 1 h. The reaction mixture was filtered through Celite, and the crystalline product was obtained after a slow gas-liquid diffusion of Et$_2$O into filtrate at 0 °C for overnight. Then the mother liquor was decanted, and the yellow crystals of **1**·0.5Me$_2$CO·0.5Et$_2$O composition were dried on air. These crystals partially loss solvate molecules to give yellow powder of **1**·0.4Me$_2$CO. Yield: 62 mg (85%). Anal. Calcd for C$_{156}$H$_{154}$B$_2$Cu$_2$N$_4$P$_4$·0.4C$_3$H$_6$O (2380.76): C, 79.3; H, 6.6 N, 2.3. Found: C, 79.0; H, 6.6; N, 2.3. ^{1}H NMR (500 MHz, DMSO-d_6, ppm) δ 7.97 (s, 4H, Ph), 7.51 (ddd, J = 14.6, 8.9,

4.0 Hz, 6H, Ph), 7.39–7.23 (m, 20H, Ph), 7.23–7.16 (m, 19H, Ph), 7.07 (dtd, J = 15.9, 7.5, 3.7 Hz, 17H, Ph), 6.93 (t, J = 7.4 Hz, 19H, Ph), 6.82–6.76 (m, 9H, Ph), 3.40 (q, J = 7.0 Hz, 4H, Im), 2.73–2.59 (m, 8H, C$\underline{H}$(CH$_3$)$_2$), 1.10 (dt, J = 6.9, 3.5 Hz, 24H, CH(C$\underline{H}_3$)$_2$), 0.76 (s, 24H, CH(C$\underline{H}_3$)$_2$). ^{13}C NMR (126 MHz, DMSO-d_6, ppm) δ 165.30 (C−Cu), 146.43 (Ph), 136.89 (Ph), 135.66 (Ph), 133.72 (Ph), 132.21 (Ph), 130.40 (Ph), 126.62 (Ph), 125.70 (Ph), 122.83 (N$\underline{C}$H), 82.27 (C−Cu), 29.62 ($\underline{C}$H(CH$_3$)$_2$), 25.30 (CH($\underline{C}$H$_3$)$_2$), 24.47 (CH($\underline{C}$H$_3$)$_2$). ^{31}P{^{1}H} NMR (202 MHz, DMSO-d_6, ppm) δ −7.45 (s). FT-IR (KBr, cm^{-1}): 420 (w), 473 (w), 486 (m), 501 (m), 515 (s), 538 (w), 550 (w), 608 (s), 623 (m), 694 (vs), 704 (vs), 733 (s), 743 (vs), 760 (m), 804 (m), 914 (vw), 943 (w), 970 (vw), 999 (w), 1032 (w), 1043 (w), 1063 (w), 1096 (m), 1121 (m), 1148 (w), 1161 (w), 1182 (w), 1211 (w), 1269 (w), 1308 (w), 1327 (m), 1348 (w), 1364 (w), 1385 (m), 1400 (m), 1437 (s), 1466 (m), 1479 (m), 1560 (w), 1580 (m), 1815 (vw), 1883 (vw), 1956 (vw), 2868 (m), 2926 (m), 2965 (m), 2997 (m), 3034 (m), 3055 (m), 3121 (w), 3146 (vw).

Complex [Ag$_2$(IPr)$_2$(μ$_4$-tpbz)](BPh$_4$)$_2$ (**2**) was prepared in a similar way using [Ag(IPr)Cl] (27.0 mg, 0.051 mmol), 1,2,4,5-tetrakis(diphenylphosphino)benzene (21.0 mg, 0.026 mmol), NaBPh$_4$ (18.0 mg, 0.052 mmol) and CH$_2$Cl$_2$ (2 mL) as solvent. It was crystallized as solvate **2**·CH$_2$Cl$_2$·Et$_2$O (yellow crystals), which quickly loss solvate molecules to give yellow powder of **2**. Yield: 50 mg (80%). Anal. Calcd for C$_{156}$H$_{154}$B$_2$Ag$_2$N$_4$P$_4$ (2446.17): C, 76.6; H, 6.3; N, 2.3. Found: C, 76.4; H, 6.3; N, 2.4. ^{1}H NMR (500 MHz, DMSO-d_6, ppm) δ 8.01 (s, 4H, Im), 7.55 (t, J = 7.7 Hz, 4H, Ph), 7.29 (t, J = 7.2 Hz, 18H, , Ph), 7.21 (tdt, J = 6.2, 2.6, 1.4 Hz, 21H, Ph), 7.06 (dt, J = 15.1, 7.5 Hz, 18H, Ph), 6.93 (t, J = 7.4 Hz, 20H, Ph), 6.85–6.72 (m, 13H, Ph), 2.61–2.51 (m, 8H, C$\underline{H}$(CH$_3$)$_2$), 1.10 (d, J = 6.8 Hz, 24H, CH(C$\underline{H}_3$)$_2$), 0.80 (d, J = 7.0 Hz, 24H, CH(C$\underline{H}_3$)$_2$). ^{13}C NMR (126 MHz, DMSO-d_6, ppm) δ 164.46 (C−Ag), 145.60 (Ph), 136.03 (Ph), 132.83 (Ph), 131.18 (Ph), 129.54 (Ph), 125.76 (Ph), 125.74 (Ph), 124.69 (Ph), 121.96 (N$\underline{C}$H), 79.00 (C−Ag), 28.66 ($\underline{C}$H(CH$_3$)$_2$), 24.22 (CH($\underline{C}$H$_3$)$_2$), 24.06 (CH($\underline{C}$H$_3$)$_2$). ^{31}P{^{1}H} NMR (202 MHz, DMSO-d_6, ppm) δ −5.41 (dd, $^1J_{31P-109/107Ag}$ = 260 and 236 Hz) and −0.09 (dd, $^1J_{31P-109/107Ag}$ = 265 and 230 Hz). FT-IR (KBr, cm^{-1}): 471 (w), 486 (w), 515 (m), 604 (m), 611 (m), 621 (m), 692 (vs), 704 (vs), 733 (s), 743 (s), 804 (m), 843 (w), 914 (vw), 935 (w), 945 (w), 968 (vw), 999 (w), 1032 (w), 1061 (w), 1096 (m), 1119 (w), 1134 (w), 1161 (w), 1182 (w), 1213 (w), 1269 (w), 1306 (w), 1327 (m), 1364 (m), 1385 (m), 1406 (m), 1437 (s), 1460 (m), 1468 (m), 1479 (m), 1557 (w), 1580 (m), 1661 (vw), 1811 (vw), 1881 (vw), 1950 (vw), 2868 (m), 2926 (m), 2963 (s), 3034 (m), 3055 (m), 3121 (w), 3148 (w).

Complex [Ag$_2$(IMes)$_2$(μ$_4$-tpbz)](BPh$_4$)$_2$ (**3**) was prepared in a similar way using [Ag(IMes)Cl] (38.5 mg, 0.086 mmol), 1,2,4,5-tetrakis(diphenylphosphino)benzene (35 mg, 0.043 mmol) and NaBPh$_4$ (29.4 mg, 0.086 mmol) in CH$_2$Cl$_2$ (3 mL). It was crystallized as solvate **3**·Et$_2$O (yellow crystals), which quickly loss solvate molecules to give yellow powder of **3**. Yield: 74 mg (76%). Anal. Calcd for C$_{144}$H$_{130}$Ag$_2$B$_2$N$_4$P$_4$ (2277.85): C, 75.9; H, 5.7; N, 2.4. Found: C, 75.9; H, 5.9; N, 2.6. ^{1}H NMR (500 MHz, DMSO-d_6, ppm) δ 7.31 (dq, J = 8.0, 4.4, 3.8 Hz, 10H, Ph), 7.20 (dddt, J = 6.6, 5.2, 2.6, 1.4 Hz, 18H, Ph), 7.16–7.07 (m, 10H, Ph), 6.99 (t, J = 7.5 Hz, 10H, Ph), 6.96–6.89 (m, 22H, Ph), 6.80 (q, J = 7.1, 6.2 Hz, 10H, Ph), 6.46 (dq, J = 42.0, 6.4 Hz, 10H, Ph), 4.06 (s, 4H, Im), 2.37 (s, 6H, CH$_3$), 2.22 (d, J = 7.2 Hz, 12H, CH$_3$), 1.97 (d, J = 37.5 Hz, 6H, CH$_3$), 1.84 (s, 12H, CH$_3$). ^{13}C NMR (126 MHz, DMSO-d_6, ppm) δ 164.45 (C−Ag), 164.05 (Ph), 163.66 (Ph), 138.22 (Ph), 136.02 (Ph), 135.71 (Ph), 129.47 (Ph), 125.74 (Ph), 121.97 (N$\underline{C}$H), 79.76 (C−Ag), 17.93 (CH$_3$), 17.29 (CH$_3$). ^{31}P{^{1}H} NMR (202 MHz, DMSO-d_6, ppm) δ −3.51 (dd, $^1J_{31P-109/107Ag}$ = 89.5 and 18.0 Hz) and −4.75 (dd, $^1J_{31P-109/107Ag}$ = 87.0 and 17.9 Hz). FT-IR (KBr, cm^{-1}): 419 (w), 473 (m), 484 (m), 511 (s), 536 (w), 575 (w), 602 (m), 610 (m), 623 (m), 692 (vs), 706 (vs), 731 (s), 743 (s), 851 (m), 908 (w), 928 (w), 970 (w), 999 (m), 1030 (m), 1067 (w), 1096 (m), 1117 (m), 1144 (w), 1159 (w), 1182 (w), 1240 (w), 1267 1287 (w), 1308 (w), 1325 (w), 1377 (m), 1404

(m), 1437 (s), 1479 (s), 1580 (m), 1609 (w), 1813 (w), 1884 (w), 1942 (vw), 2855 (w), 2918 (w), 2982 (m), 2997 (m), 3013 (m), 3032 (m), 3053 (m), 3127 (w), 3157 (w), 3169 (vw).

Complex $[Au_2(IPr)_2(\mu_4\text{-tpbz})](BPh_4)_2 \cdot 0.8CH_2Cl_2$ ($4 \cdot 0.8CH_2Cl_2$) was prepared in a similar way using [Au(IPr)Cl] (21.0 mg, 0.034 mmol), 1,2,4,5-tetrakis(diphenylphosphino)benzene (14.0 mg, 0.017 mmol) and NaBPh$_4$ (11.7 mg, 0.034 mmol) in CH_2Cl_2 (2 mL). The reaction mixture was filtered through Celite, and the dark yellow crystals of $4 \cdot CH_2Cl_2 \cdot Et_2O$ were obtained after a slow gas-liquid diffusion of Et$_2$O into filtrate at 0 °C for overnight. Under air-handling, solvate $4 \cdot CH_2Cl_2 \cdot Et_2O$ partially loss solvate molecules to give dark yellow powder of $4 \cdot 0.8CH_2Cl_2$. Yield: 20 mg (43%). Anal. Calcd for $C_{156}H_{154}Au_2B_2N_4P_4 \cdot 0.8CH_2Cl_2$ (2692.31): C, 70.0; H, 5.8; N, 2.1; Found: C, 70.2; H, 6.0; N, 2.0. ^1H NMR (500 MHz, DMSO-d_6, ppm) δ 8.21–8.06 (m, 4H, Im), 7.61 (td, J = 7.7, 7.0, 4.0 Hz, 4H, Ph), 7.38–7.24 (m, 17H, Ph), 7.24–7.12 (m, 17H, Ph), 7.03 (q, J = 6.4 Hz, 17H, Ph), 6.92 (t, J = 7.3 Hz, 16H, Ph), 6.78 (t, J = 7.2 Hz, 8H, Ph), 6.19 (q, J = 6.2 Hz, 15H, Ph), 2.59 (h, J = 6.9 Hz, 8H, C$\underline{H}$(CH$_3$)$_2$), 1.11 (d, J = 6.8 Hz, 24H, CH(C$\underline{H}_3$)$_2$), 0.85 (d, J = 6.8 Hz, 24H, CH(C$\underline{H}_3$)$_2$). ^{13}C NMR (126 MHz, DMSO-d_6, ppm) δ 164.45 (C−Au), 145.57 (Ph), 136.03 (Ph), 134.80 (Ph), 132.87 (Ph), 131.35 (Ph), 129.54 (Ph), 125.76 (Ph), 124.85 (Ph), 121.97 (N$\underline{C}$H), 81.42 (C−Au), 28.76 ($\underline{C}$H(CH$_3$)$_2$), 24.45 (CH($\underline{C}$H$_3$)$_2$), 23.62 (CH($\underline{C}$H$_3$)$_2$). $^{31}P\{^1H\}$ NMR (202 MHz, DMSO-d_6, ppm) δ 24.64 (s). FT-IR (KBr, cm^{-1}): 473 (w), 496 (m), 517 (m), 606 (s), 611 (m), 623 (m), 692 (vs), 704 (vs), 733 (s), 743 (s), 804 (m), 843 (w), 945 (w), 999 (w), 1032 (w), 1061 (w), 1097 (m), 1121 (w), 1136 (w), 1182 (w), 1213 (w), 1258 (w), 1269 (w), 1288 (w), 1308 (w), 1329 (m), 1364 (w), 1385 (m), 1414 (m), 1437 (s), 1458 (m), 1468 (m), 1479 (s), 1558 (w), 1580 (m), 1811 (w), 1881 (w), 1944 (w), 2868 (m), 2926 (m), 2963 (s), 2999 (m), 3034 (m), 3055 (s), 3121 (w), 3148 (w).

Complex $[Au_2(IPr)_2(\mu_3\text{-tpbz})](BPh_4)_2 \cdot 0.9CH_3CN$ ($5 \cdot 0.9CH_3CN$) was prepared in a similar way using [Au(IPr)Cl] (25.0 mg, 0.040 mmol), 1,2,4,5-tetrakis(diphenylphosphino)benzene (17.0 mg, 0.021 mmol) and NaBPh$_4$ (14.0 mg, 0.041 mmol) in CH_3CN (2 mL). The reaction mixture was filtered through Celite, and the yellow crystals of $5 \cdot 6CH_3CN$ were obtained after a slow gas-liquid diffusion of Et$_2$O into filtrate at 0 °C for overnight. Under air-handling, solvate $5 \cdot 6CH_3CN$ partially loss solvate molecules to give yellow powder of $5 \cdot 0.9CH_3CN$. Yield: 50 mg (91%). Anal. Calcd for $C_{156}H_{154}Au_2B_2N_4P_4 \cdot 0.9CH_3CN$ (2661.31): C, 71.2; H, 5.9; N, 2.6. Found: C, 71.2; H, 6.0; N, 2.4. ^1H NMR (500 MHz, DMSO-d_6, ppm) δ 8.19–8.06 (m, 4H, Im), 7.61 (td, J = 7.7, 7.0, 4.0 Hz, 4H, Ph), 7.42–7.24 (m, 17H, Ph), 7.24–7.13 (m, 17H, Ph), 7.03 (q, J = 6.4 Hz, 17H, Ph), 6.92 (t, J = 7.3 Hz, 16H, Ph), 6.78 (t, J = 7.2 Hz, 8H, Ph), 6.19 (q, J = 6.2 Hz, 15H, Ph), 2.59 (h, J = 6.9 Hz, 8H, C$\underline{H}$(CH$_3$)$_2$), 1.11 (d, J = 6.8 Hz, 24H, CH(C$\underline{H}_3$)$_2$), 0.85 (d, J = 6.8 Hz, 24H, CH(C$\underline{H}_3$)$_2$). ^{13}C NMR (126 MHz, DMSO-d_6, ppm) δ 165.44 (C−Au), 146.40 (Ph), 136.84 (Ph), 135.62 (Ph), 133.74 (Ph), 132.14 (Ph), 130.35 (Ph), 126.57 (Ph), 125.63 (Ph), 122.76 (N$\underline{C}$H), 80.24 (C−Au), 29.57 ($\underline{C}$H(CH$_3$)$_2$), 25.30 (CH($\underline{C}$H$_3$)$_2$), 24.44 (CH($\underline{C}$H$_3$)$_2$). $^{31}P\{^1H\}$ NMR (202 MHz, DMSO-d_6, ppm) δ 25.10 (s). FT-IR (KBr, cm^{-1}): 473 (w), 496 (w), 517 (m), 550 (w), 567 (w), 606 (m), 611 (m), 623 (m), 692 (s), 704 (vs), 733 (s), 743 (s), 760 (m), 806 (m), 843 (w), 912 (vw), 937 (w), 947 (w), 974 (w), 999 (w), 1032 (w), 1043 (w), 1061 (w), 1099 (m), 1121 (w), 1132 (w), 1159 (w), 1182 (w), 1215 (w), 1258 (w), 1269 (w), 1308 (w), 1329 (w), 1364 (w), 1385 (w), 1437 (s), 1468 (m), 1479 (m), 1553 (w), 1580 (m), 1630 (w), 1813 (vw), 1884 (vw), 1952 (vw), 2868 (m), 2926 (m), 2963 (vs), 2999 (m), 3034 (s), 3055 (s), 3117 (w), 3142 (m), 3154 (w).

§3. Single crystal X-ray crystallography

Diffraction data for single crystals of **1**·0.5Me$_2$CO·0.5Et$_2$O, **2**·CH$_2$Cl$_2$·Et$_2$O, **3**·Et$_2$O, **4**·CH$_2$Cl$_2$·Et$_2$O, **5**·6MeCN, were collected on an automated Agilent Xcalibur diffractometer equipped with an area AtlasS2 detector (graphite monochromator, λ(MoKα) = 0.71073 Å, ω-scans with a step of 0.5°). Integration, absorption correction, and determination of unit cell parameters were performed using the CrysAlisPro program package.[7] Data collection, integration, and determination of unit cell parameters were performed using APEX2, APEX3 and SAINT software, absorption correction was applied based on the intensities of equivalent reflections with the use of SADABS.[8] The structures were solved by dual space algorithm (SHELXT)[9] and refined by the full-matrix least squares technique (SHELXL)[10] in the anisotropic approximation (except hydrogen atoms). Positions of hydrogen atoms of organic ligands were calculated geometrically and refined in the riding model. The crystallographic data and details of the structure refinements are summarized in Table S1. CCDC 2164284–2164288 contain the supplementary crystallographic data for this paper. These data can be obtained free of charge from The Cambridge Crystallographic Data Center at https://www.ccdc.cam.ac.uk/structures/.

Table S1. X-Ray crystallographic data for **1**–**5**.

	1·0.5Me$_2$CO·0.5Et$_2$O	**2**·CH$_2$Cl$_2$·Et$_2$O	**3**·Et$_2$O	**4**·CH$_2$Cl$_2$·Et$_2$O	**5**·6MeCN
CCDC number	2164284	2164285	2164288	2164286	2164287
Empirical formula	C$_{159.5}$H$_{162}$B$_2$Cu$_2$N$_4$OP$_4$	C$_{161}$H$_{166}$Ag$_2$B$_2$Cl$_2$N$_4$OP$_4$	C$_{148}$H$_{140}$Ag$_2$B$_2$N$_4$OP$_4$	C$_{161}$H$_{166}$Au$_2$B$_2$Cl$_2$N$_4$OP$_4$	C$_{168}$H$_{172}$Au$_2$B$_2$N$_{10}$P$_4$
M, g/mol	2423.50	2605.11	2351.87	2783.30	2870.58
Crystal system	Monoclinic	Monoclinic	Triclinic	Monoclinic	Triclinic
Space group	$P2_1/c$	$P2_1/n$	$P\overline{1}$	$P2_1/n$	$P\overline{1}$
a, b, c, Å	18.3234(2), 15.9847(3), 47.2050(8)	22.5068(4), 18.6930(3), 34.6520(7)	12.1495(2), 15.3578(4), 18.6160(5)	22.4140(5), 18.7123(3), 34.3946(6)	12.67455(17), 18.2029(2), 32.1344(4)
α, β, γ, °	93.8679(12)	106.636(2)	113.461(3), 99.1447(19), 97.457(2)	105.895(3)	80.182(1), 88.7727(11), 82.1319(10)
V, Å^3	13794.6(4)	13968.6(5)	3073.60(14)	13874.1(5)	7236.48(16)
Z	4	4	1	4	2
D(calc.), g/cm^3	1.167	1.239	1.271	1.332	1.317
μ, mm^{-1}	0.41	0.42	0.43	2.25	2.13
F(000)	5132	5464	1228	5720	2956
Crystal size, mm	0.35 × 0.29 × 0.09	0.30 × 0.16 × 0.13	0.39 × 0.22 × 0.15	0.41 × 0.14 × 0.04	0.34 × 0.15 × 0.05
Reflections collected/ independent	62267 / 26153	81174 / 28295	23688 / 14005	74271 / 29341	55927 / 30994
R_{int}	0.024	0.024	0.019	0.032	0.028
Reflections with $I > 2σ(I)$	20968	21981	11893	21969	25970
Goodness-of-fit on F^2	1.059	1.053	1.077	1.030	1.037
Final R indices [$I > 2σ(I)$]	$R_1 = 0.0453$, $wR_2 = 0.1381$	$R_1 = 0.0414$, $wR_2 = 0.1120$	$R_1 = 0.0404$, $wR_2 = 0.1128$	$R_1 = 0.0416$, $wR_2 = 0.0925$	$R_1 = 0.0375$, $wR_2 = 0.0826$
R indices (all data)	$R_1 = 0.0606$, $wR_2 = 0.1814$	$R_1 = 0.0614$, $wR_2 = 0.0856$	$R_1 = 0.0507$, $wR_2 = 0.1128$	$R_1 = 0.0670$, $wR_2 = 0.0856$	$R_1 = 0.0506$, $wR_2 = 0.0781$
Largest diff. peak / hole, e/Å^3	0.90, -0.45	1.39, -0.94	0.72, -0.59	1.69, -0.88	1.31, -1.03
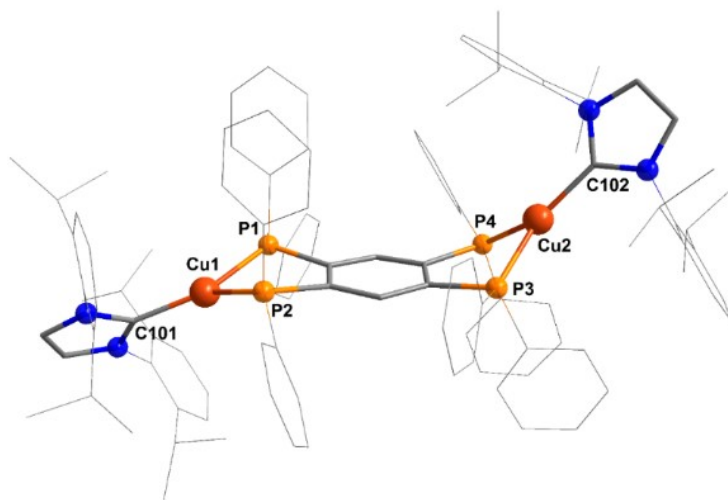
Figure S1. X-Ray derived structure of **1**·0.5Me$_2$CO·0.5Et$_2$O. The [Ph$_4$B]$^-$ anions, solvent molecules and hydrogen atoms are omitted for clarity. Selected bond lengths (Å) and angles (°): Cu1−P1 2.3270(6), Cu1−P2 2.3099(6), Cu1−C101 1.960(2), Cu2−P3 2.3010(6), Cu2−P4 2.3252(7), Cu2−C201 1.941(2), P2−Cu1−P1 86.24(2), C101−Cu1−P1 139.20(6), C101−Cu1−P2 134.55(6), P3−Cu2−P4 85.41(2), C201−Cu2−P3 135.44(7), C201−Cu2−P4 139.08(7).
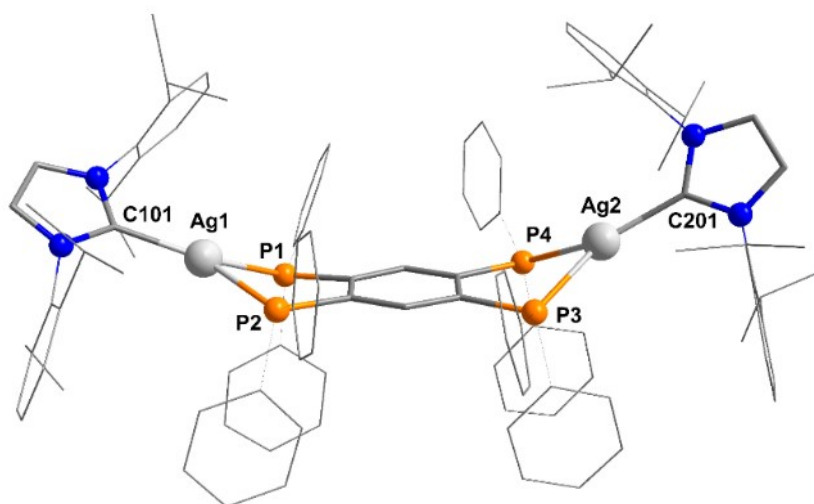

Figure S2. X-Ray derived structure of **2**·CH$_2$Cl$_2$·Et$_2$O. The [Ph$_4$B]$^-$ anions, solvent molecules and hydrogen atoms are omitted for clarity. Selected bond lengths (Å) and angles (°): Ag1−C101 2.114(2), Ag1−P1 2.5079(6), Ag1−P2 2.4807(6), Ag2−C201 2.126(2), Ag2−P3 2.5334(6), Ag2−P4 2.4979(6), C101−Ag1−P1 140.15(6), C101−Ag1−P2 139.15(6), C201−Ag2−P3 137.20(6), C201−Ag2−P4 143.71(6), P1−Ag1−P2 80.39(2), P3−Ag2−P4 79.08(2).
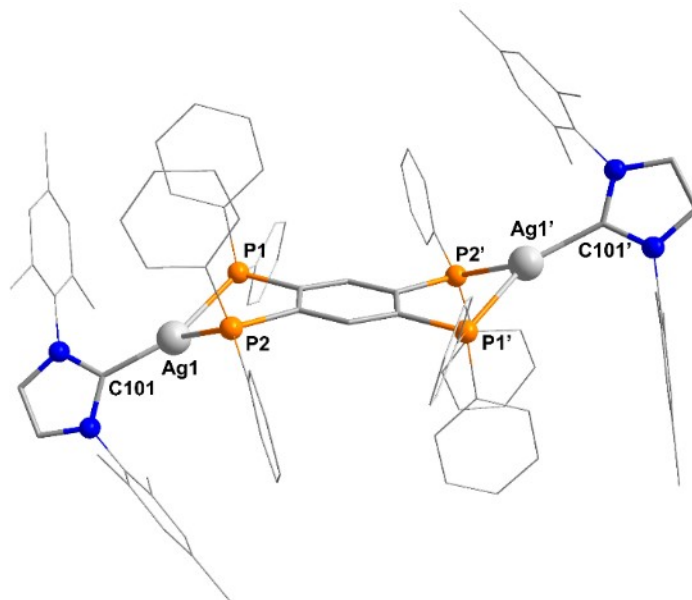
Figure S3. X-Ray derived structure of **3**·Et$_2$O. The [Ph$_4$B]$^-$ anions, solvent molecules and hydrogen atoms are omitted for clarity. Selected bond lengths (Å) and angles (°): Ag1−C101 2.097(2), Ag1−P1 2.4783(6), Ag1−P2 2.4777(6), C101−Ag1−P1 142.31(7), C101−Ag1−P2 136.85(7), P2−Ag1−P1 80.220(19). Symmetry code: (′) 1−x, 1−y, −z.

Figure S4. X-Ray derived structure of **4**·CH$_2$Cl$_2$·Et$_2$O. The [Ph$_4$B]$^-$ anions, solvent molecules and hydrogen atoms are omitted for clarity. The gold atoms are disordered over the positions (**Au1/Au1′** and **Au2/Au2′**) with the relative occupancies of **Au1/Au1′** = 0.534:0.466 and **Au2/Au2′** = 0.941:0.059. Selected bond lengths (Å) and angles (°): Au1−C101 2.019(3), Au1−P1 2.626(4), Au1−P2 2.332(2), Au2−C201 2.044(3), Au2−P3 2.7994(8), Au2−P4 2.3072(8), Au1′−C101 2.076(4), Au1′−P1 2.403(4), Au1′−P2 2.446(3), Au2′−C201 2.083(4), Au2′−P3 2.264(3), Au2′−P4 2.772(4), C101−Au1−P1 130.5(2), C101−Au1−P2 149.9(3), P2−Au1−P1 79.57(8), C201−Au2−P3 122.71(9), C201−Au2−P4 160.05(10), P4−Au2−P3 77.15(3), C101−Au1′−P1 141.2(2), C101−Au1′−P2 136.5(2), P1−Au1′−P2 81.99(7), C201−Au2′−P3 157.8(3), C201−Au2′−P4 123.4(2), P3−Au2′−P4 78.40(9).
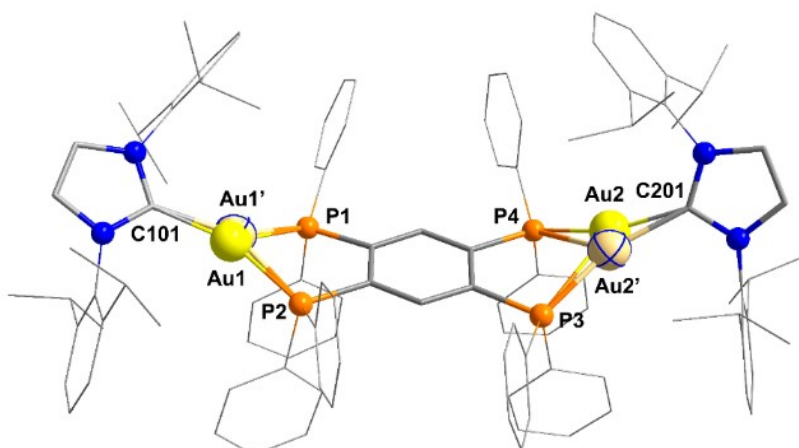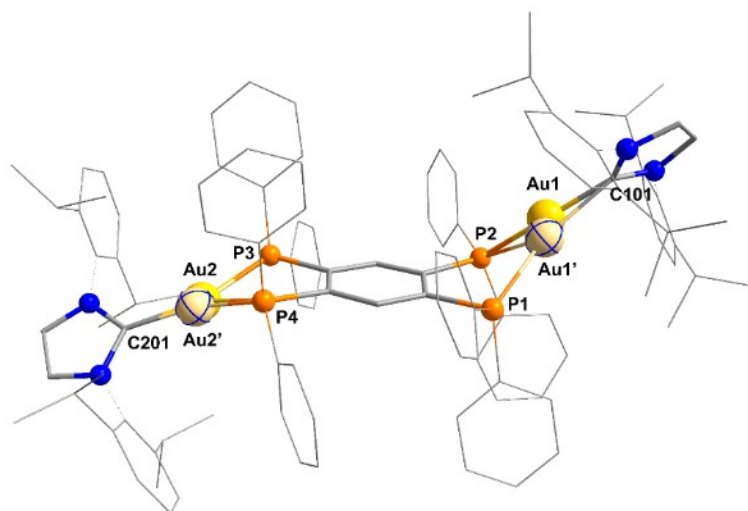
Figure S5. X-Ray derived structure of **5**·6MeCN. The [Ph₄B]⁻ anions, solvent molecules and hydrogen atoms are omitted for clarity. The gold atoms are disordered over the positions (**Au1/Au1′** and **Au2/Au2′**) with the relative occupancies of **Au1/Au1′** = 0.9717:0.0283 and **Au2/Au2′** = 0.5020:0.4980. Selected bond lengths (Å) and angles (°): Au1−P1 3.2371(8), Au1−P2 2.2918(7), Au1−C101 2.026(3), Au2−P3 2.423(2), Au2−P4 2.442(2), Au2−C201 2.109(3), Au2'−P3 2.773(4), Au2'−P4 2.2921 (16) Au2'−C201 2.012 (3), C101−Au1−P2 169.25(8), P3−Au2−P4 83.46 (5), C201−Au2−P3 141.84(16), C201−Au2−P4 134.60(16), P1−Au1'−P2 81.92(13), C101−Au1'−P1 150.1(3), C101−Au1'−P2 128.0(3), P4−Au2'−P3 78.85(9), C201−Au2'−P3 126.40(17), C201−Au2'−P4 154.7(2).
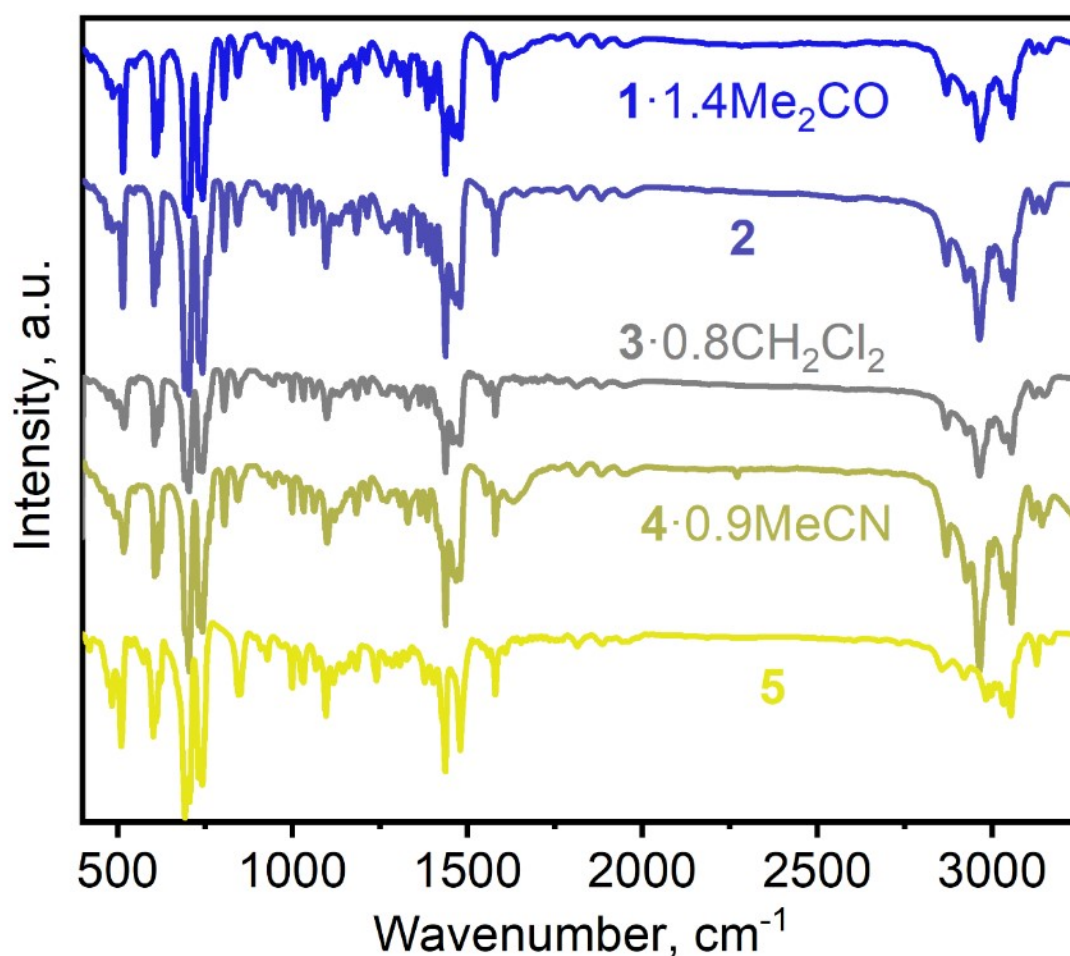
§4. FT-IR spectra

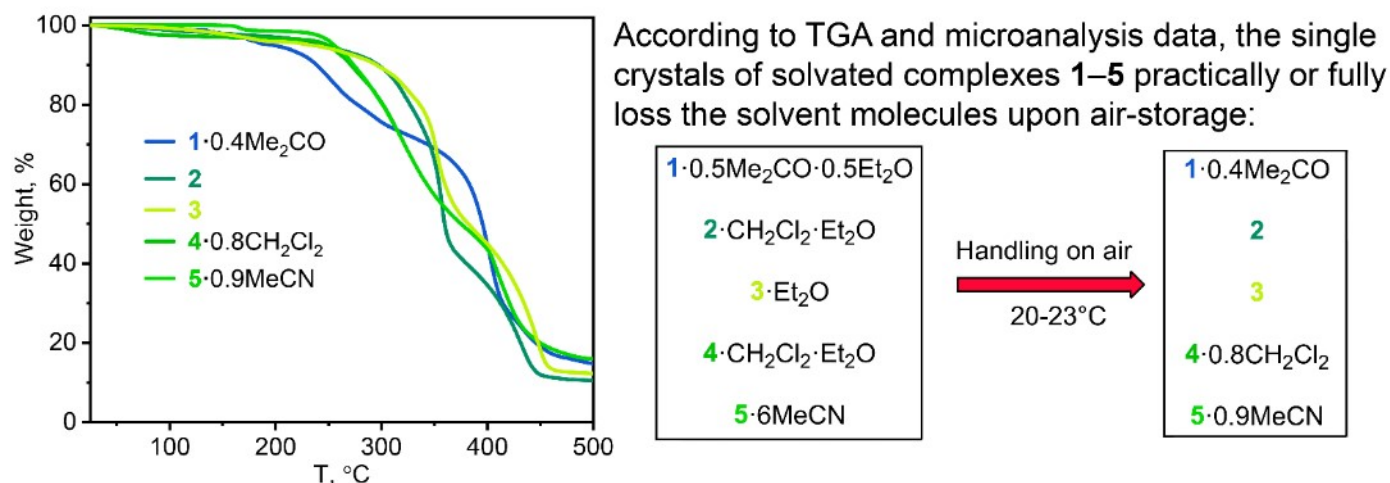**Figure S6**. *mid*-IR spectra of powder samples of **1**–**5** in KBr.

§5. TGA curves

According to TGA and microanalysis data, the single crystals of solvated complexes **1–5** practically or fully loss the solvent molecules upon air-storage:

$1 \cdot 0.5Me_2CO \cdot 0.5Et_2O$		$1 \cdot 0.4Me_2CO$
$2 \cdot CH_2Cl_2 \cdot Et_2O$	Handling on air	2
$3 \cdot Et_2O$	20-23°C	3
$4 \cdot CH_2Cl_2 \cdot Et_2O$		$4 \cdot 0.8CH_2Cl_2$
$5 \cdot 6MeCN$		$5 \cdot 0.9MeCN$

Figure S7. TGA curves for **1**–**5**.

§6. Powder X-ray diffraction data

Unit cell parameters for crystals of $1 \cdot 0.5Me_2CO \cdot 0.5Et_2O$ at 150 K	Refined parameters for powder of $1 \cdot 0.4Me_2CO$ at 298 K
$a = 18.3234(2)$, $b = 15.9847(3)$ $c = 47.2050(8)$ $\beta = 93.8679(12)$	$a = 18.44$ $b = 16.37$ $c = 47.13$ $\beta = 93.51$
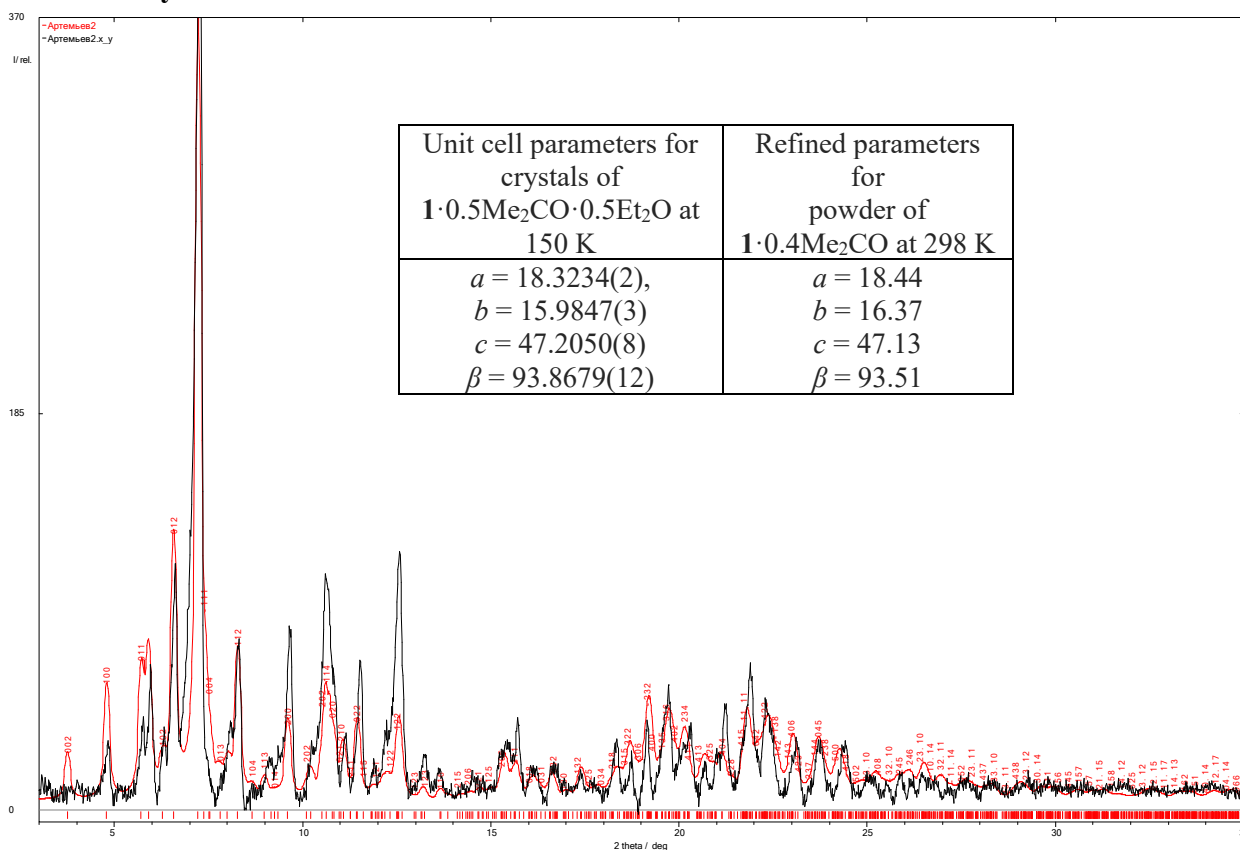
Figure S8. Comparison between the refined PXRD data for **1**·0.4Me$_2$CO and the simulated pattern for complex **1**·0.5Me$_2$CO·0.5Et$_2$O.

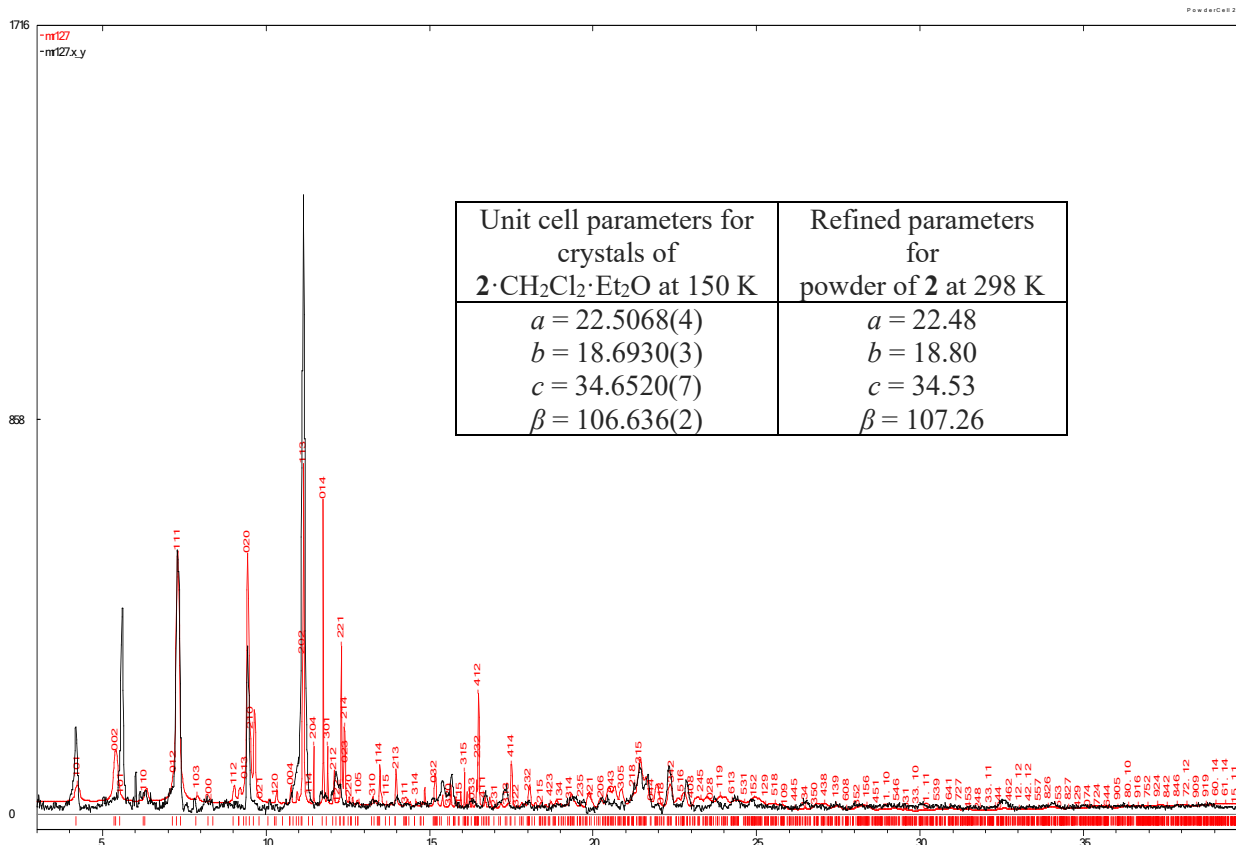**Figure S9**. Comparison between the refined PXRD data for **2** and the simulated pattern for $2 \cdot CH_2Cl_2 \cdot Et_2O$.
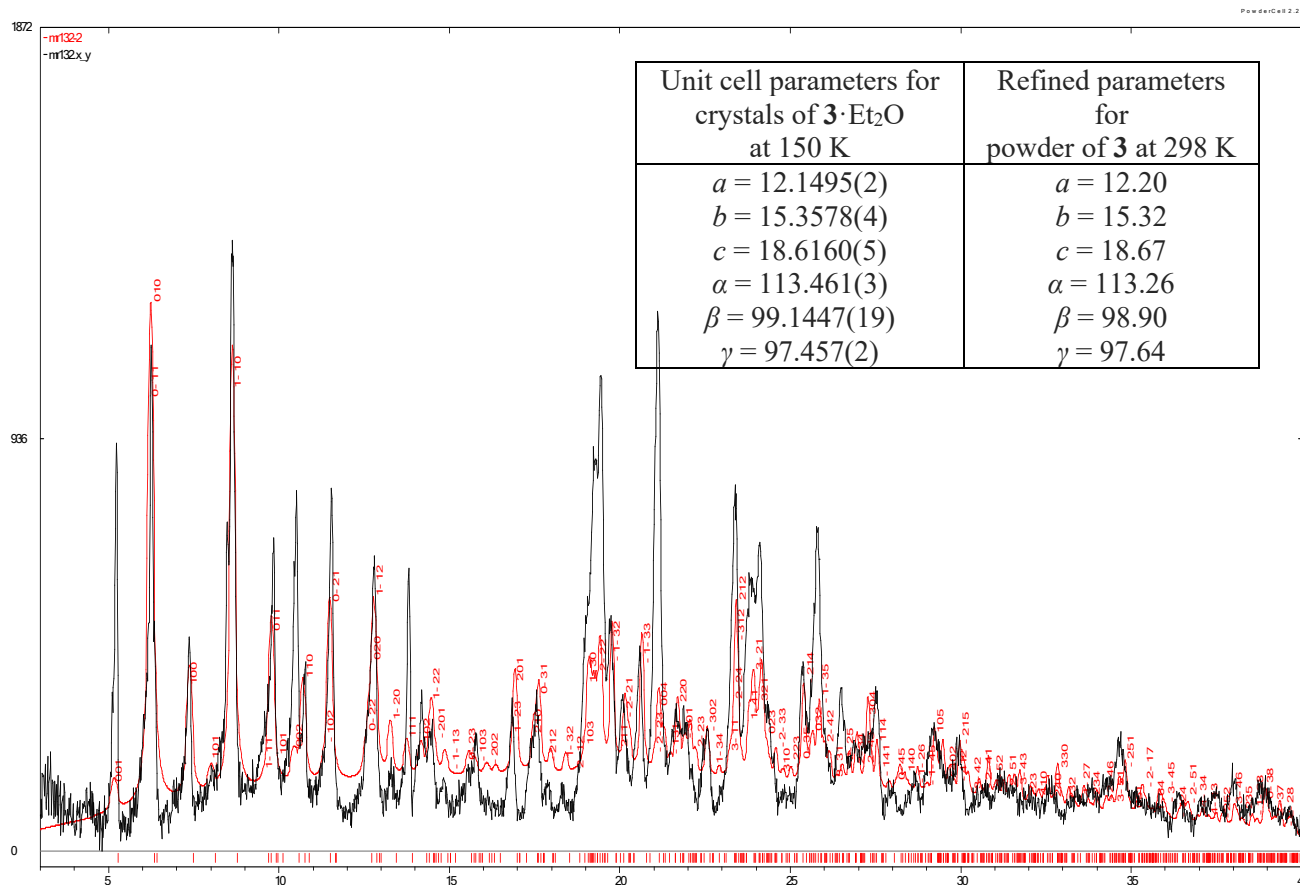
Unit cell parameters for crystals of $2 \cdot CH_2Cl_2 \cdot Et_2O$ at 150 K	Refined parameters for powder of **2** at 298 K
$a = 22.5068(4)$	$a = 22.48$
$b = 18.6930(3)$	$b = 18.80$
$c = 34.6520(7)$	$c = 34.53$
$\beta = 106.636(2)$	$\beta = 107.26$

Figure S10. Comparison between the refined PXRD data for **3** and the simulated pattern for $3 \cdot Et_2O$.

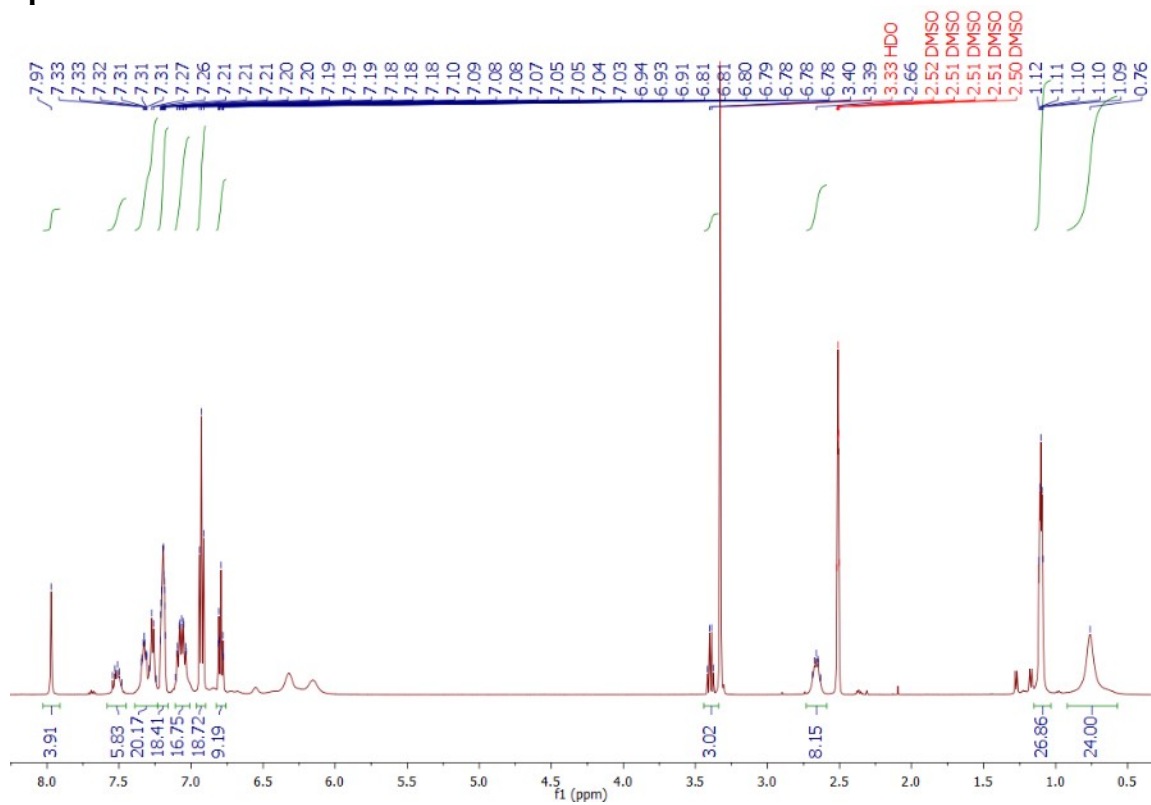| Unit cell parameters for crystals of $3 \cdot Et_2O$ at 150 K	Refined parameters for powder of **3** at 298 K
$a = 12.1495(2)$	$a = 12.20$
$b = 15.3578(4)$	$b = 15.32$
$c = 18.6160(5)$	$c = 18.67$
$\alpha = 113.461(3)$	$\alpha = 113.26$
$\beta = 99.1447(19)$	$\beta = 98.90$
$\gamma = 97.457(2)$	$\gamma = 97.64$

§7. NMR spectra

Figure S11. ¹H NMR spectrum of **1**.
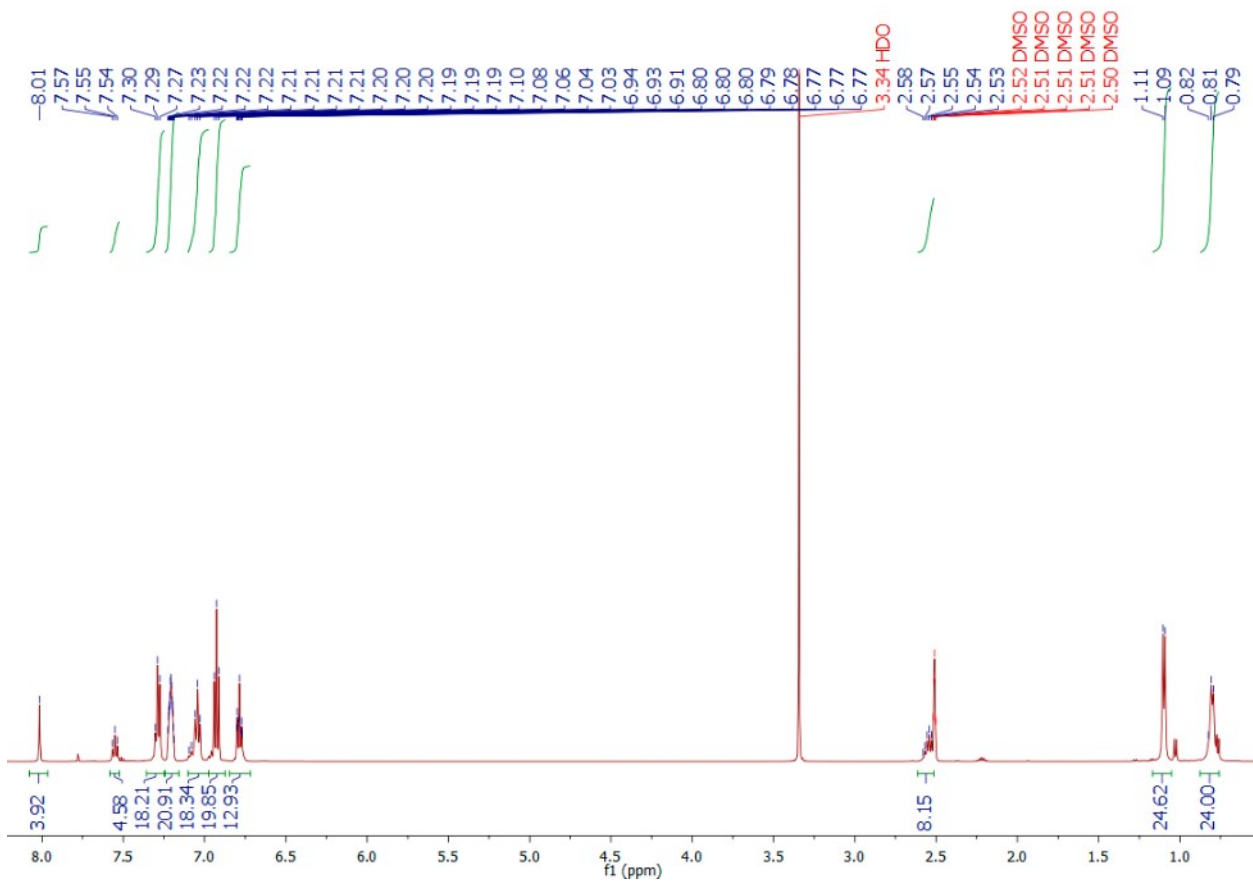
Figure S12. ¹H NMR spectrum of **2**.
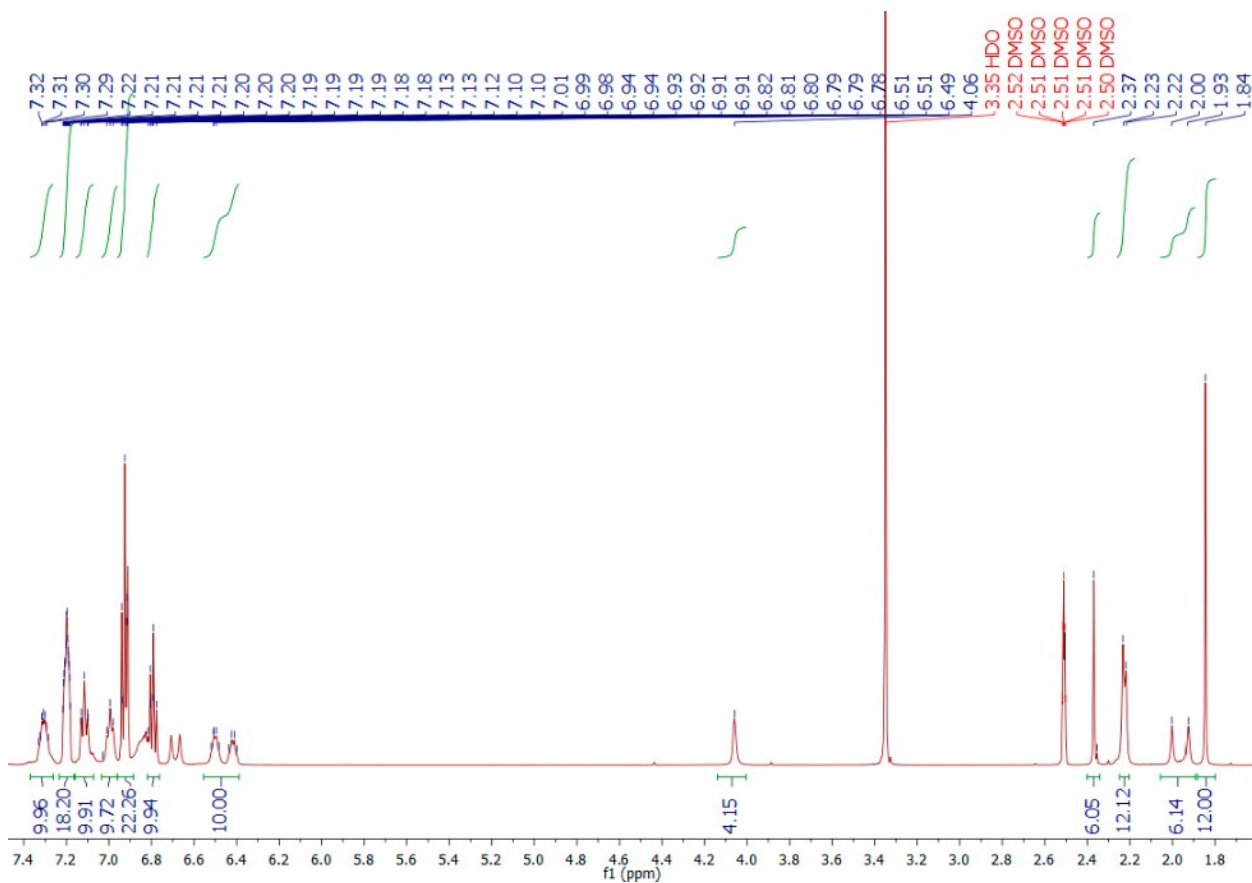
Figure S13. ^{1}H NMR spectrum of **3**.
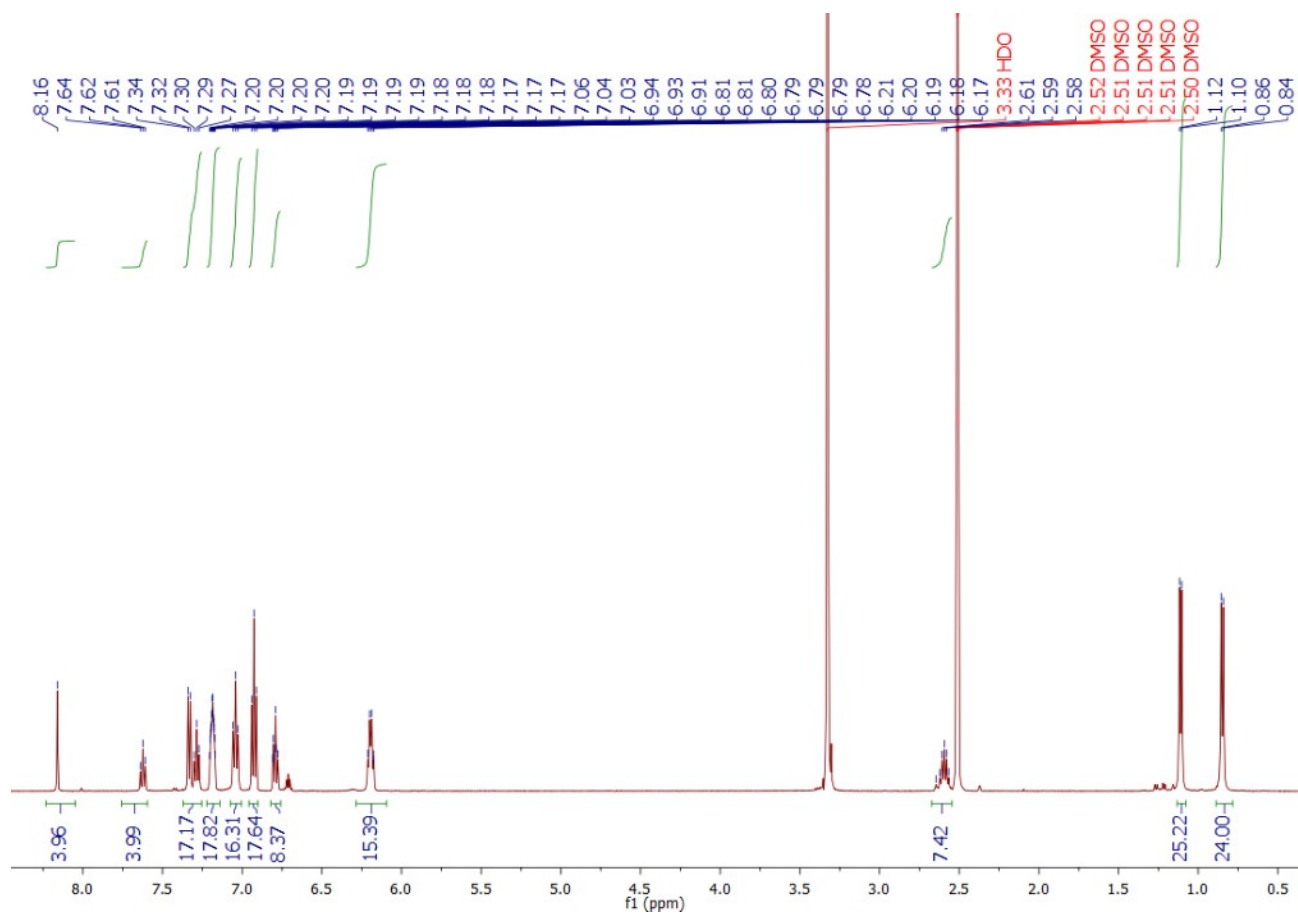
Figure S14. ^{1}H NMR spectrum of **4**.
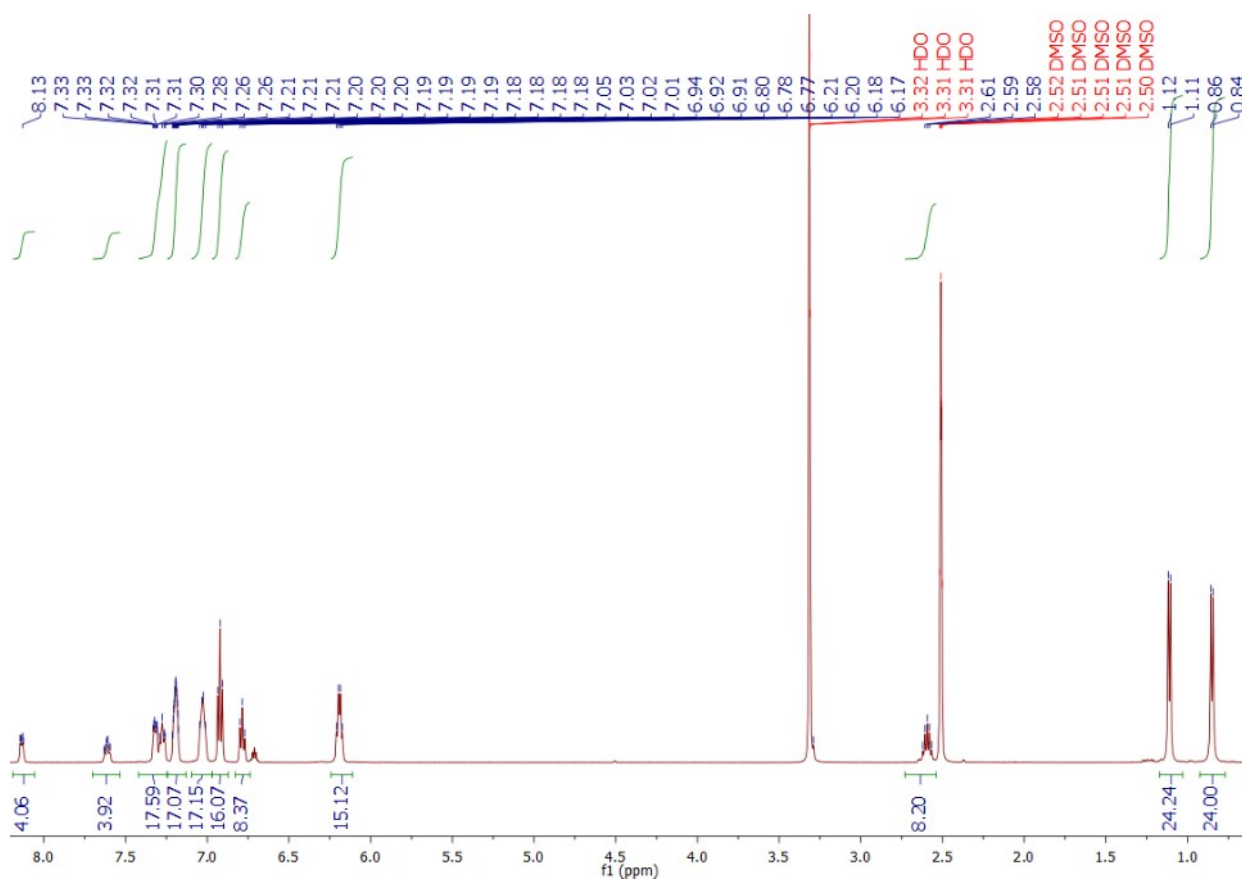
Figure S15. ^{1}H NMR spectrum of **5**.
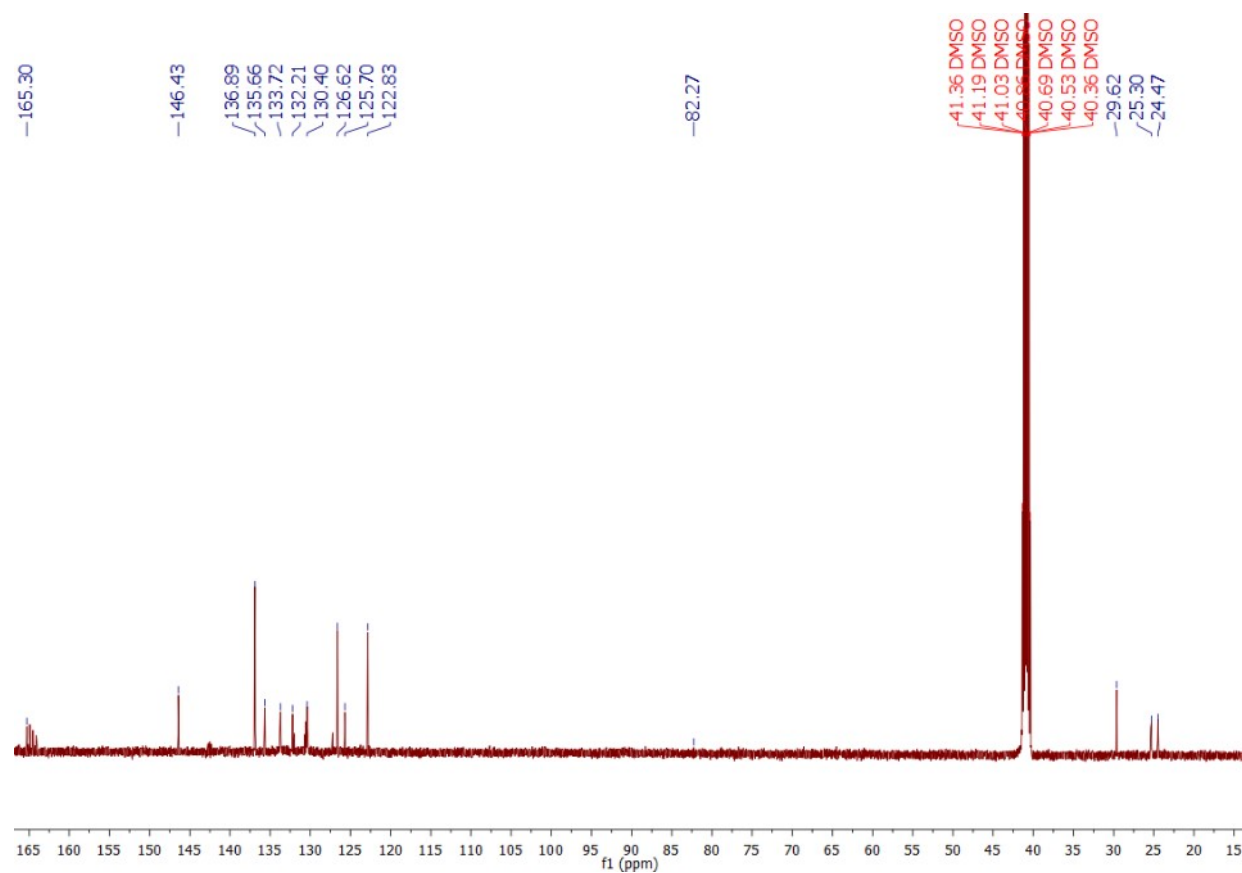
Figure S16. ^{13}C NMR spectrum of **1**.
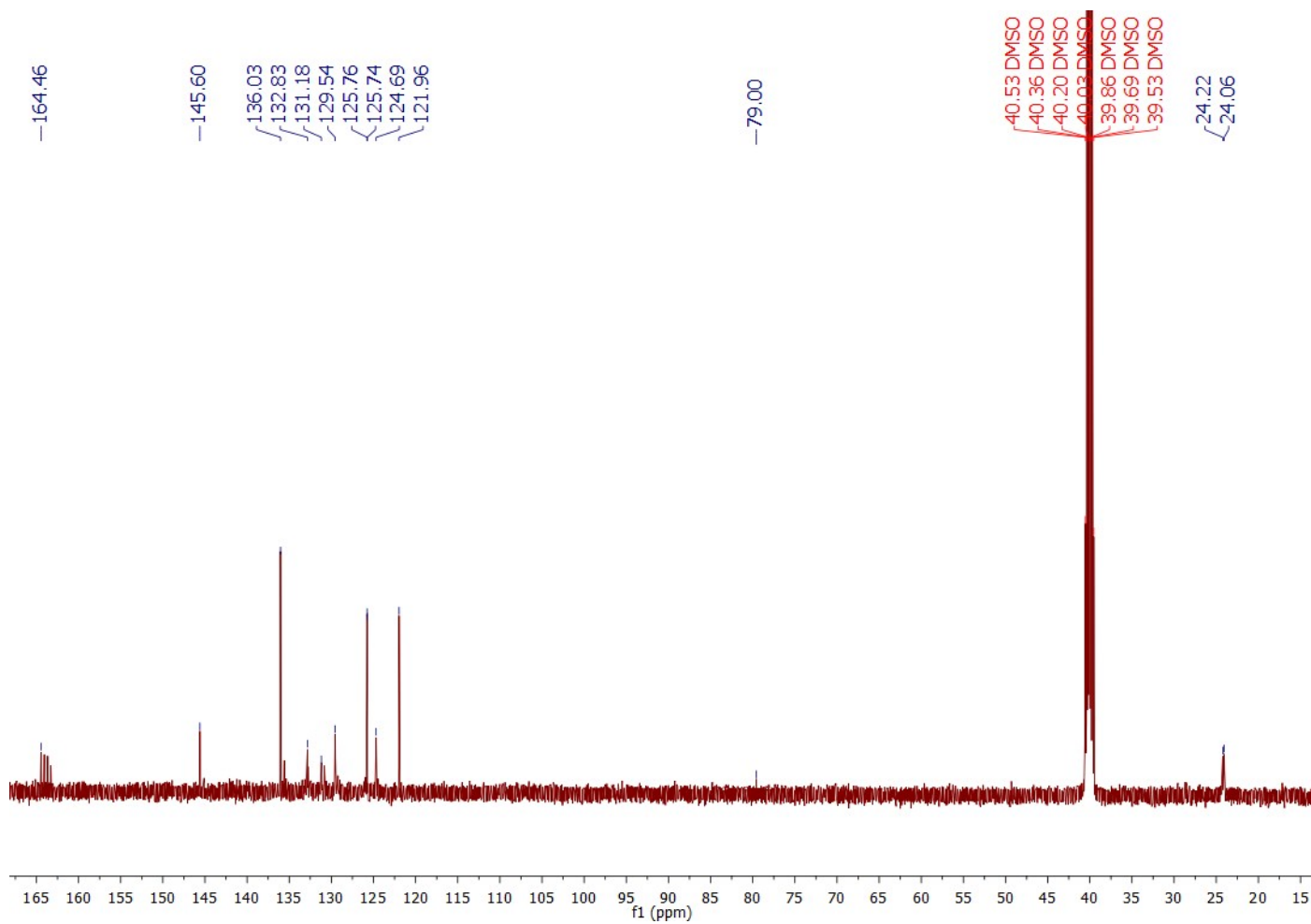
Figure S17. ^{13}C NMR spectrum of **2**.
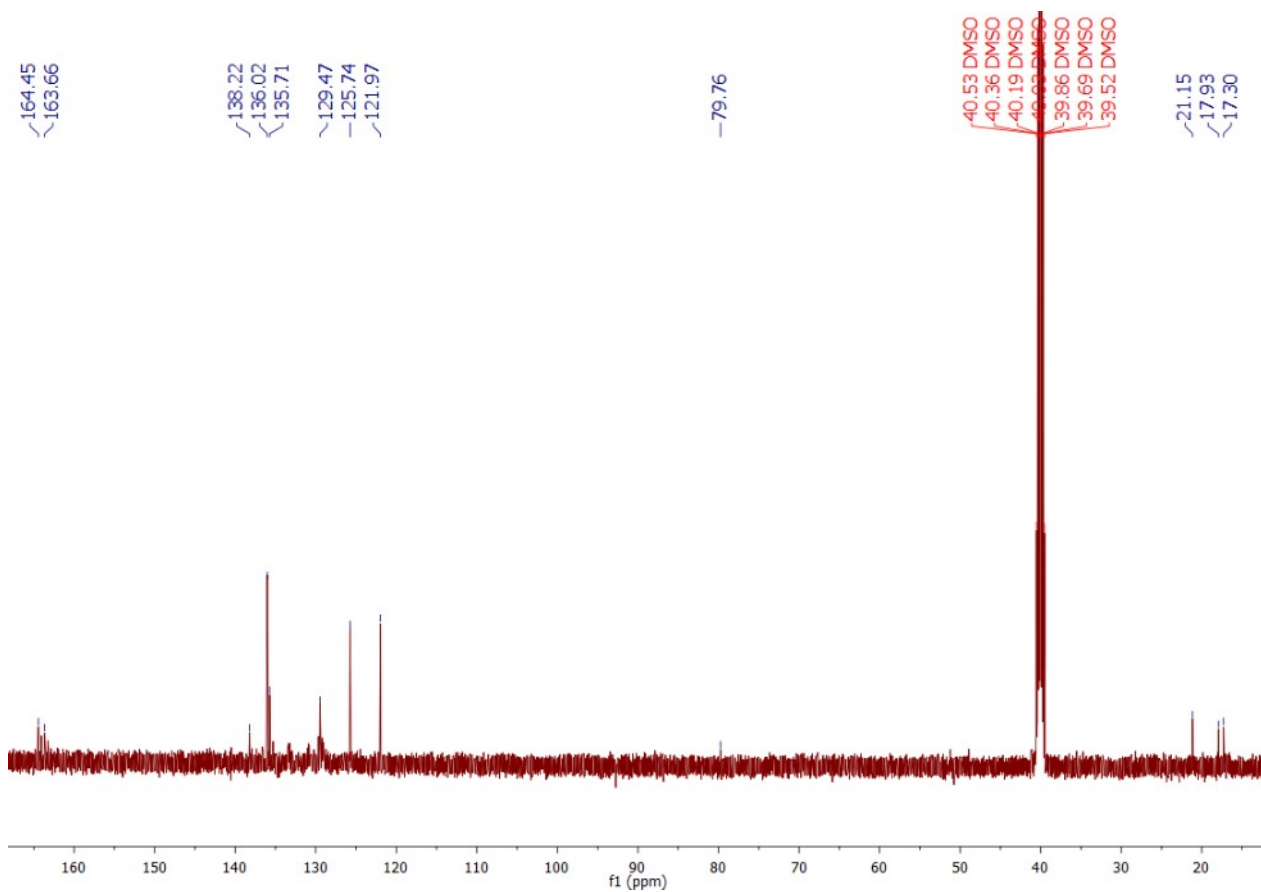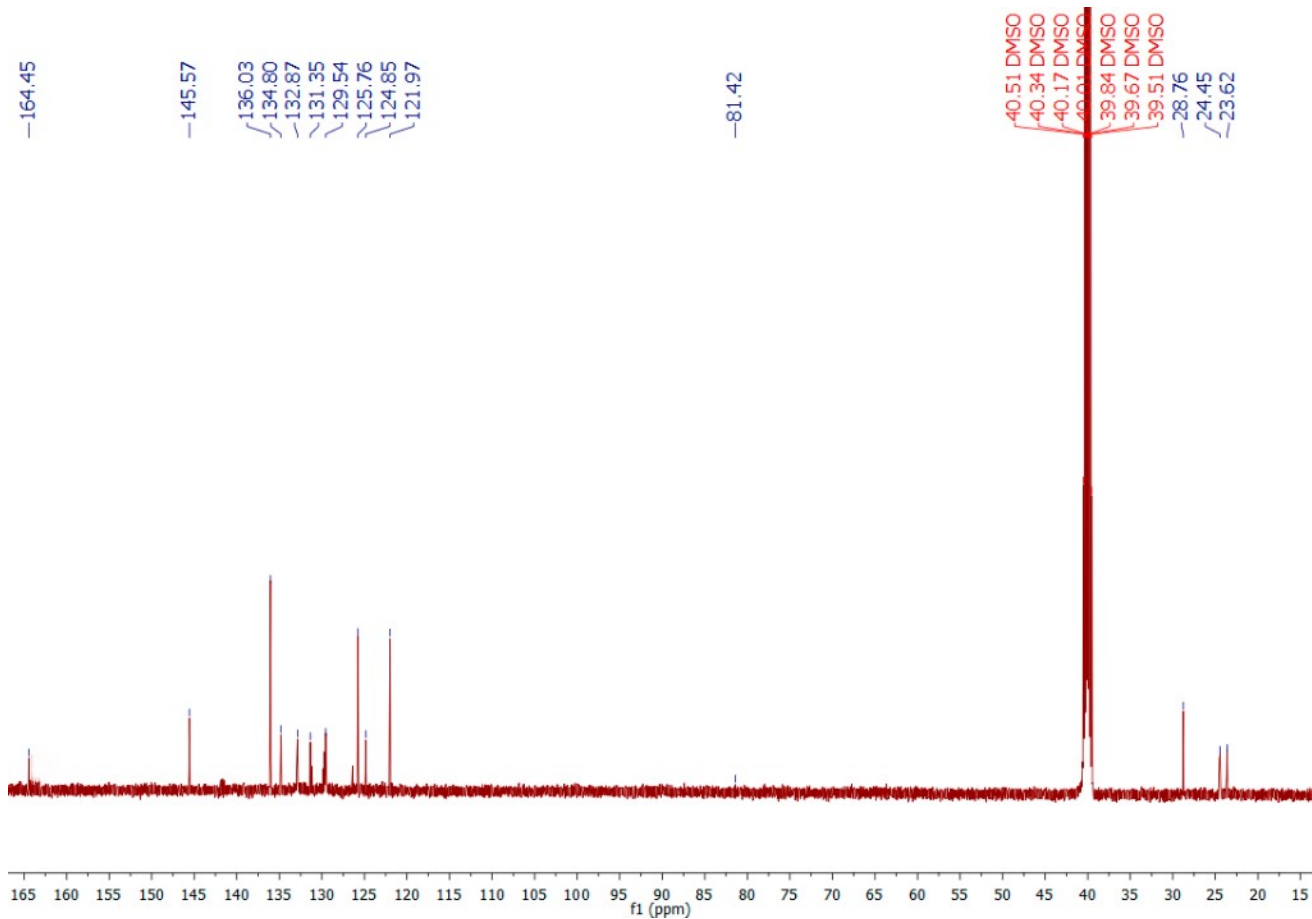

Figure S18. ^{13}C NMR spectrum of **3**.

Figure S19. ^{13}C NMR spectrum of **4**.
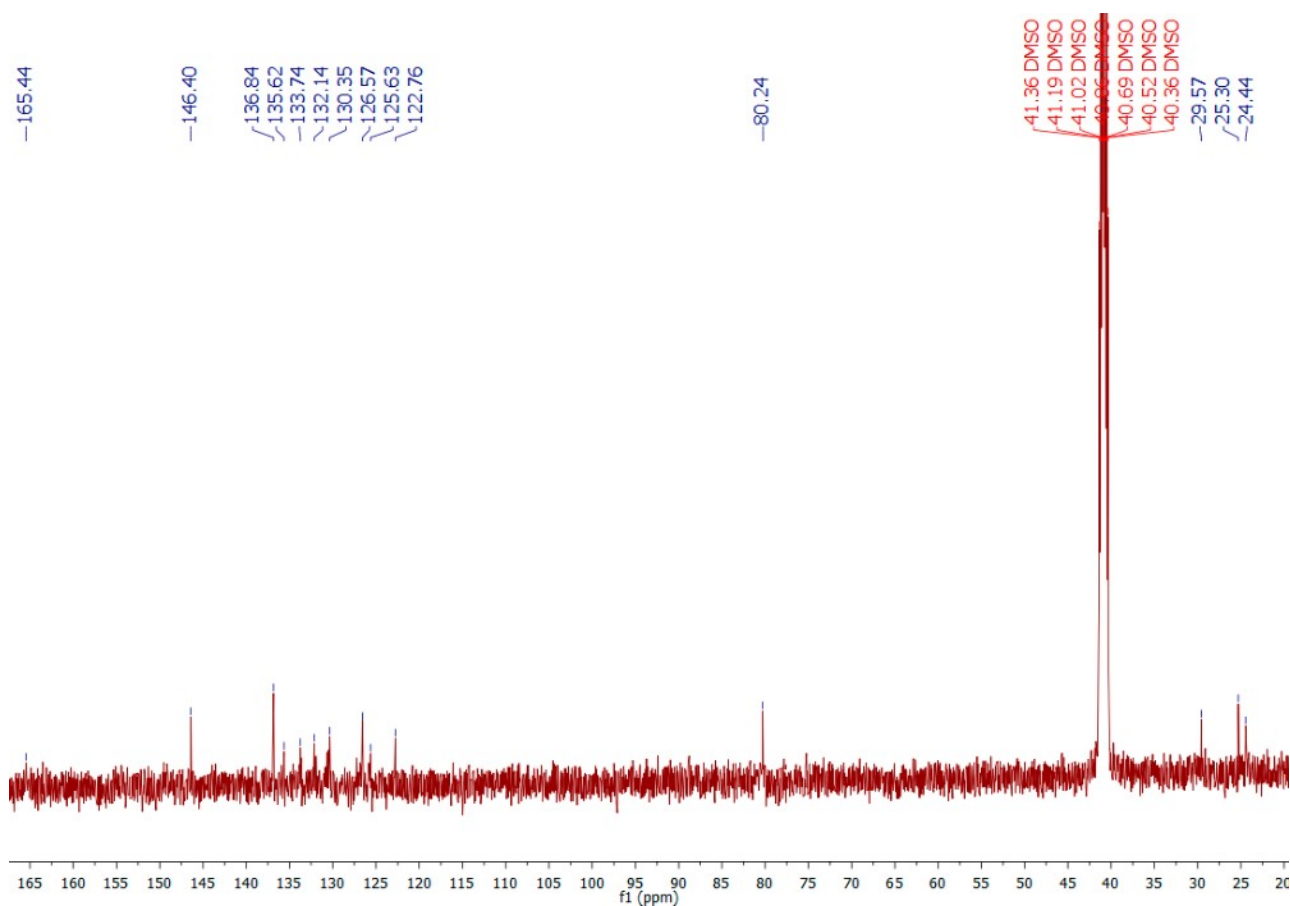
Figure S20. ^{13}C NMR spectrum of **5**.
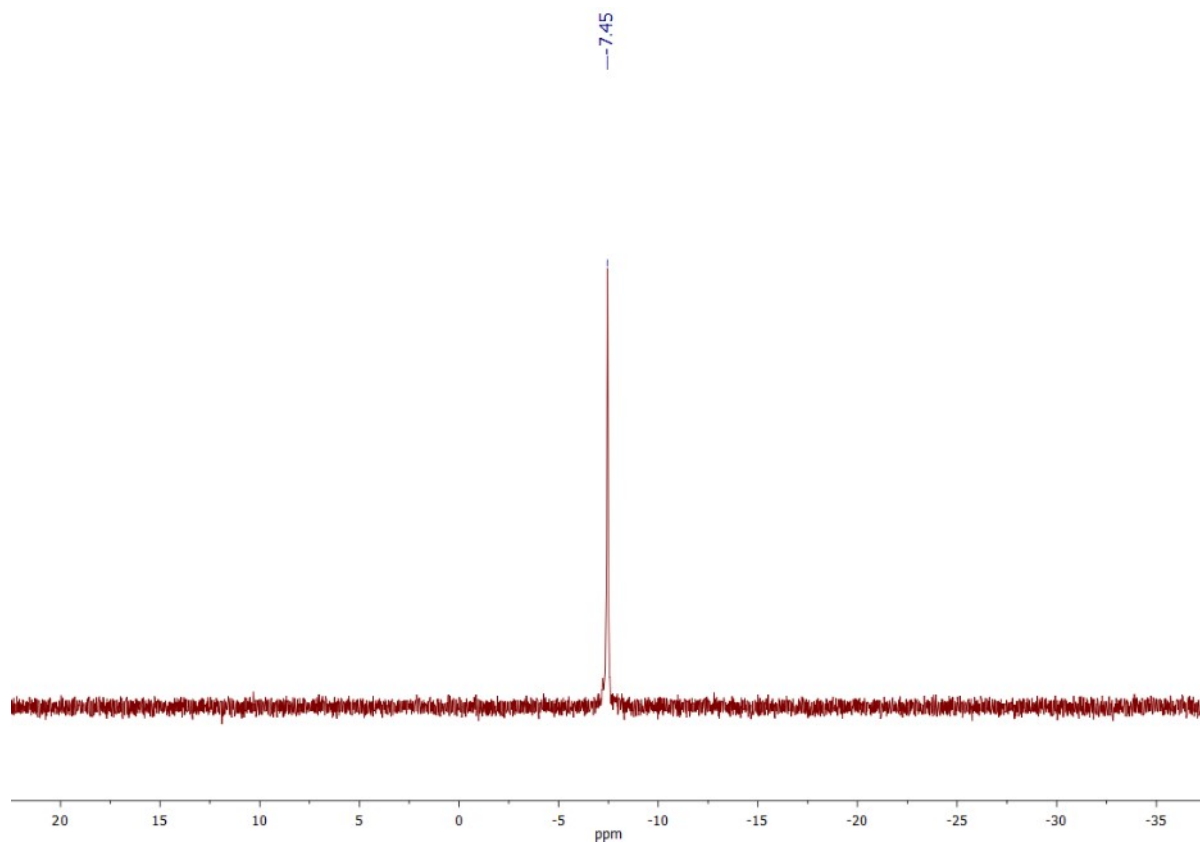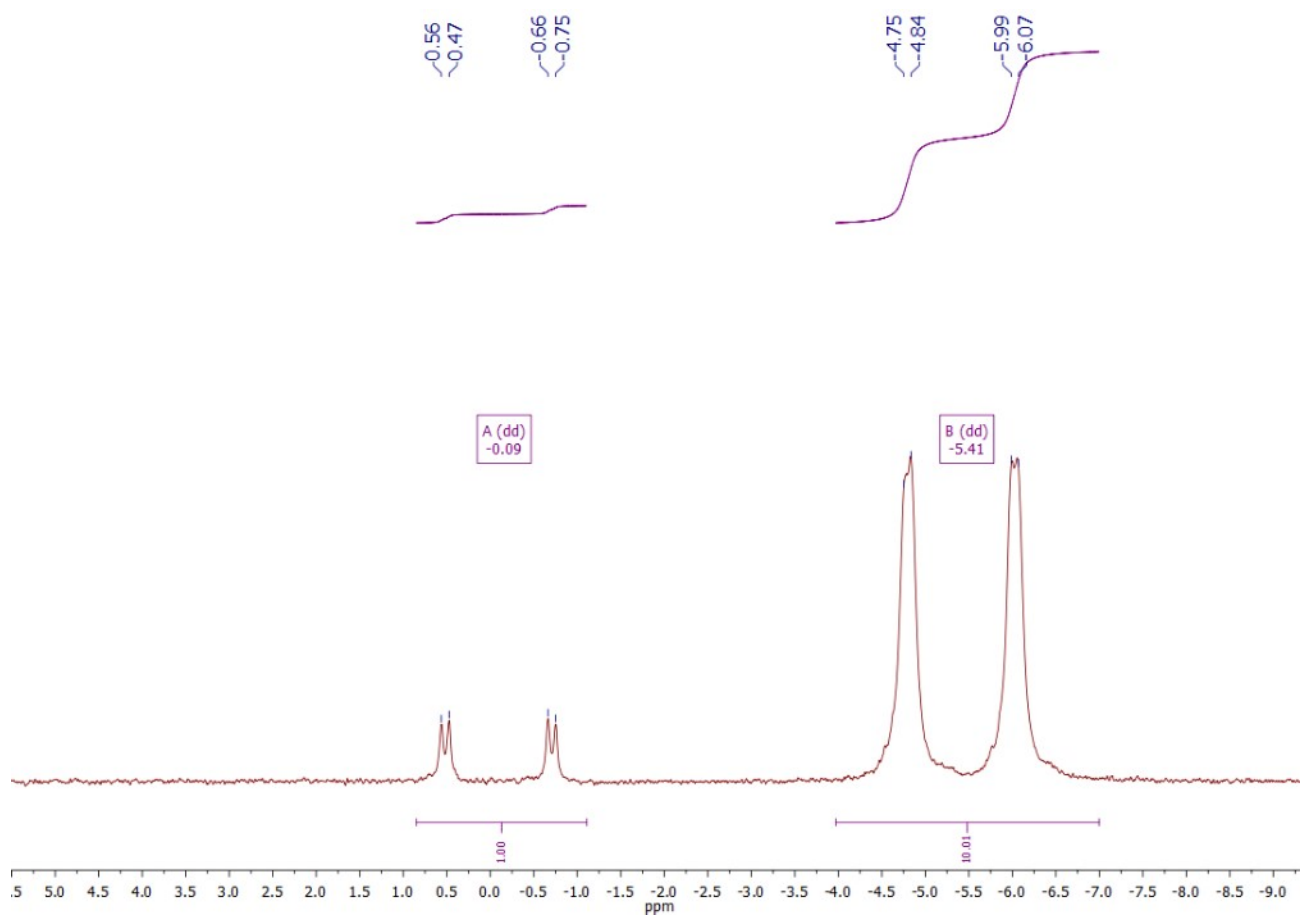
Figure S21. $^{31}P\{^1H\}$ NMR spectrum of **1**.

Figure S22. $^{31}P\{^1H\}$ NMR spectrum of **2**.
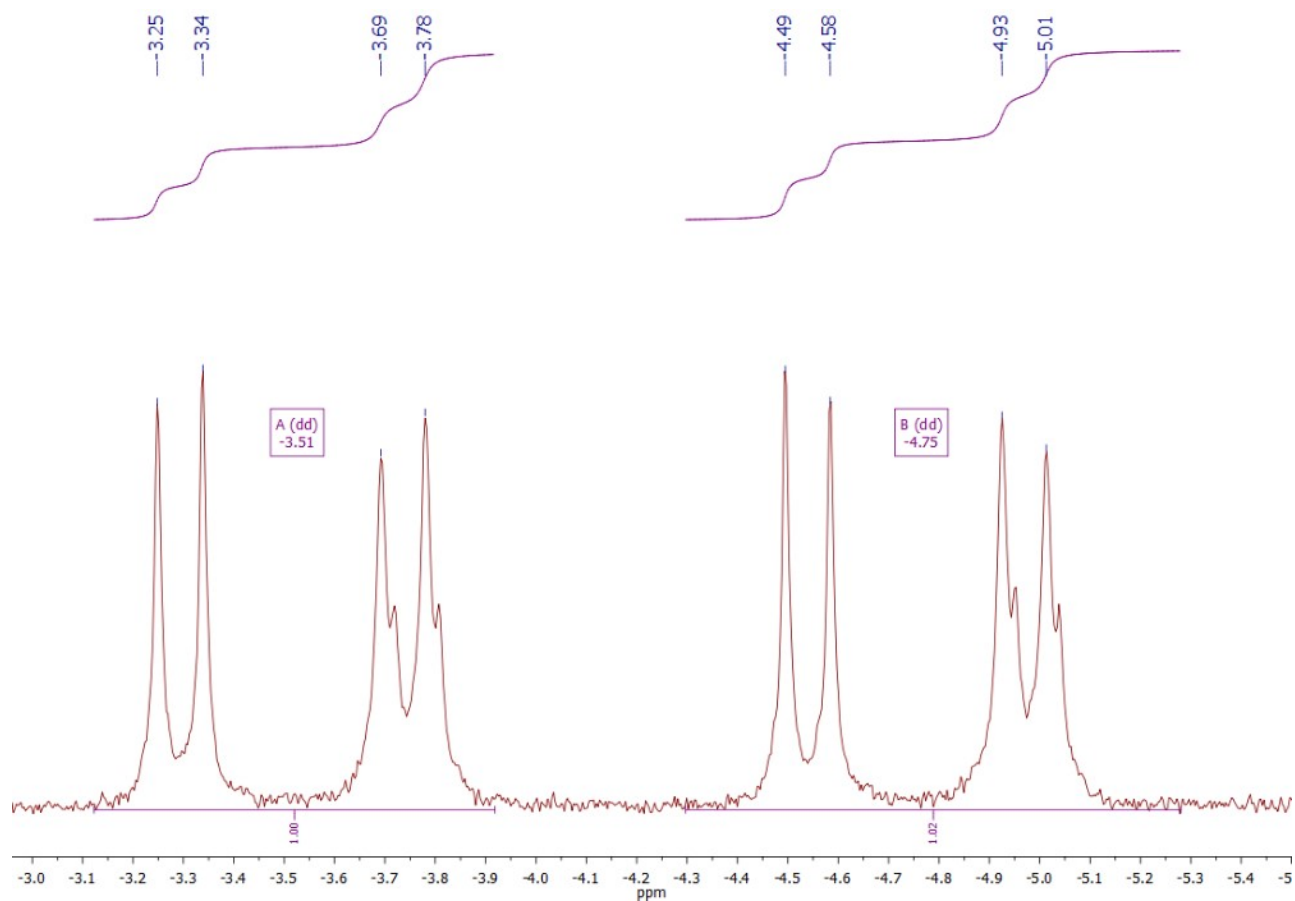
Figure S23. ^{31}P{^{1}H} NMR spectrum of **3**.
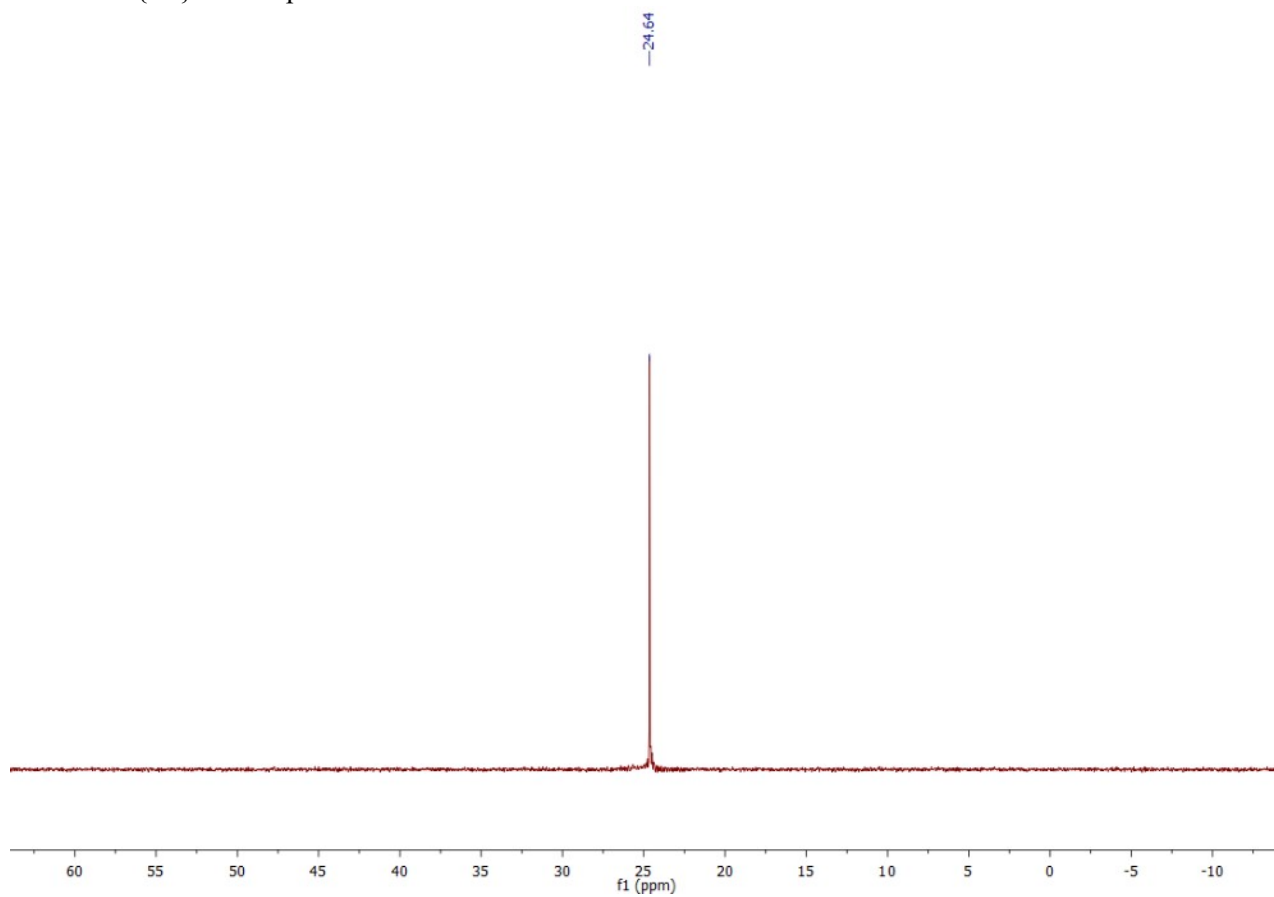
Figure S24. ^{31}P{^{1}H} NMR spectrum of **4**.
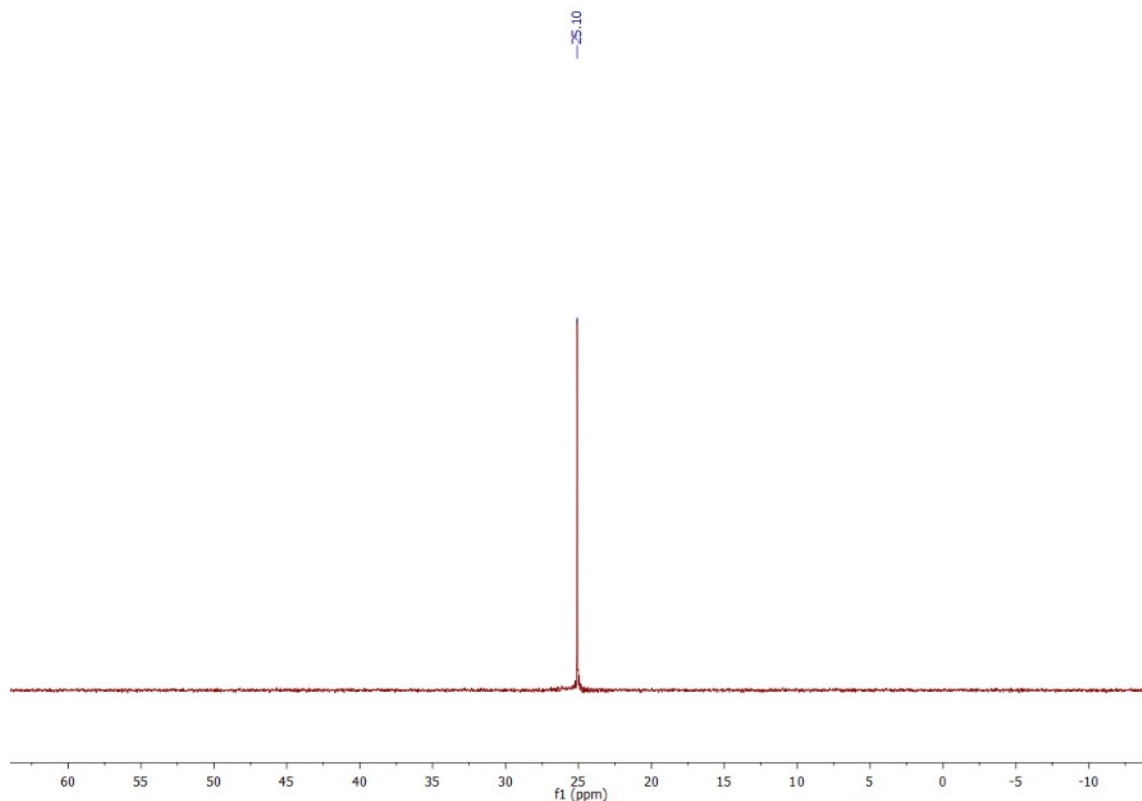
Figure S25. $^{31}P\{^1H\}$ NMR spectrum of **5**.

§7.1. Explanation of the identical spectra patterns of 4 and 5 in solution

The identical NMR, electronic absorption and luminescence spectra, as well as temperature dependences of luminescence decay time for **4** and **5** in solution testify that only one isomer, *cis*- (**4**) or *trans*- (**5**), prevails in solution. At the same time, the same isomer as in the solid state exist in solution in the case of **2** (*cis*) and **3** (*trans*). Note that DFT calculations predict that the electronic energies of the optimized *trans*-forms (**3** and **5**) are lower in solution than the *cis*-forms (**2** and **4**), with the energy difference being very small (0.3 kcal/mol) for the Ag(I) complexes (**2** and **3**) and much higher (7.7 kcal/mol) for Au(I) complexes (**4** and **5**). To prove that *cis-trans* isomerization is fast for **4**, and much slower for **2**, the localization of the transition state should be done. Unfortunately, we have not yet been able to optimize these structures due to the large size of the investigated complexes and the inability to simplify the structure without significantly affecting the isomerization barrier. Therefore, we can only put forward a hypothesis based on a simple model, for example, the Evans–Polanyi principle, according to which the difference in the activation energy of reactions of the same family is proportional to the difference in their reaction enthalpy – $E_{act} = E_0 + \alpha\Delta H$.

If $\alpha = 1$ and rate constant (k_{c-t}) of thermoneutral *cis*-trans isomerization of Ag(I) complex is very low, for example $1/k_{c-t} = 10$ days, the isomerization of Au(I) complex **4** will proceed for 20 seconds. In the case of $\alpha = 0.5$ and the same rate constant for the Ag(I) complex, the isomerization of Au(I)complex **4** will proceed within 20 minutes. If the described hypothesis with $0{,}5 \le \alpha \le 1$ is correct and the Ag(I) complexes (**2** or **3**) isomerize within a few days, then the dissolved *cis*-isomer **4** will rapidly convert to the *trans*-isomer **5**. Thus, the NMR, UV-Vis and PL spectra correspond to **5** when both **5** or **4** are dissolved.

§8. Emission decay kinetics
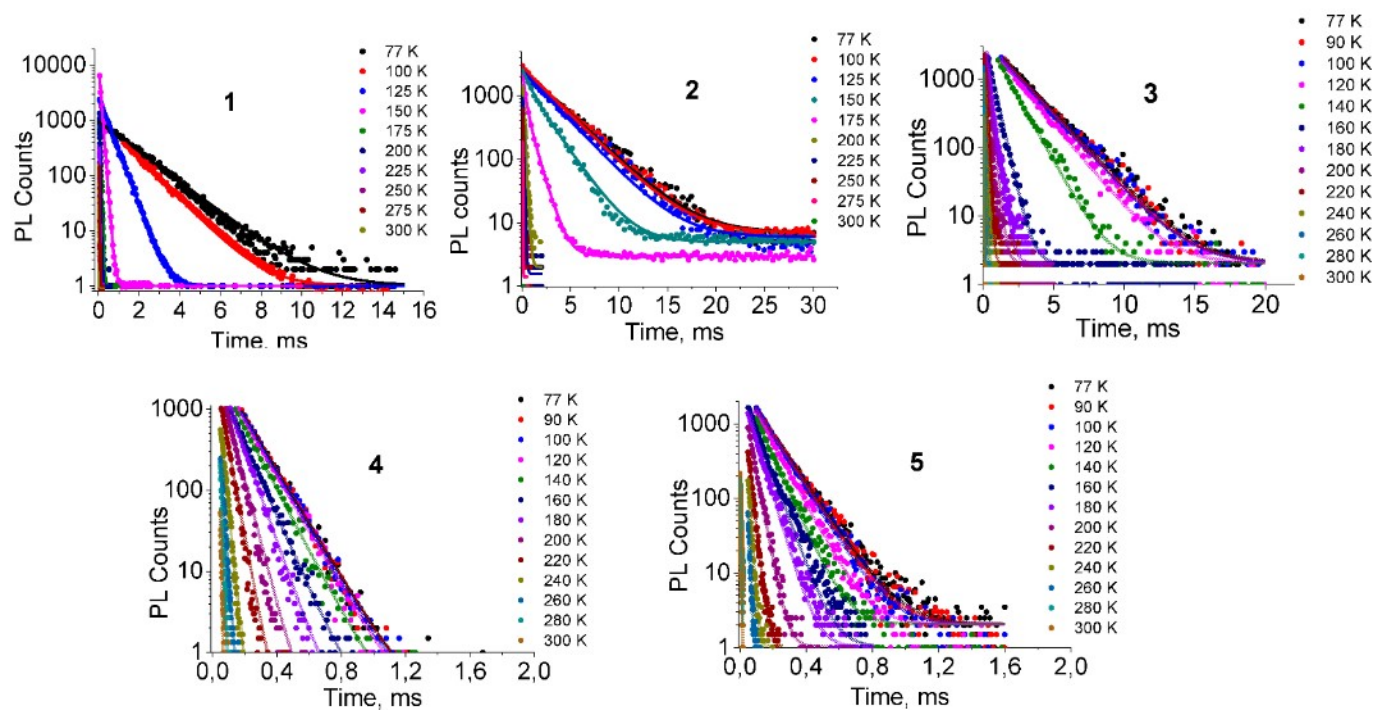
Figure S26. Emission decay kinetics for solid complexes **1**–**5** recorded at 77–298 K range.

Table S2. Emission decay times for solid complexes **1**–**5**.

1			**2**			**3**			**4**			**5**		
T, K	τ, µs	R^2	T, K	τ, µs	R^2	T, K	τ, µs	R^2	T, K	τ, µs	R^2	T, K	τ, µs	R^2
77	1692	0.997	77	3000	0.993	77	1980	0.998	77	132	0.999	77	133	0.999
100	1400	0.996	100	2913	0.998	90	1953	0.998	90	131	0.999	90	127	0.998
125	443	0.996	125	2688	0.994	100	1941	0.998	100	129	0.998	100	122	0.999
150	90	0.997	150	1491	0.998	120	1734	0.998	120	127	0.999	120	105	0.999
175	39	0.998	175	448	0.997	140	1150	0.998	140	115	0.999	140	88	0.997
200	22	0.989	200	144	0.996	160	460	0.974	160	97	0.999	160	72	0.998
225	9.6	0.985	225	75	0.996	180	273	0.909	180	77	0.999	180	59	0.998
250	4.7	0.978	250	30	0.994	200	221	0.902	200	57	0.993	200	36	0.998
275	3.0	0.981	275	15	0.994	220	100	0.998	220	40	0.998	220	22	0.997
298	2.5	0.976	298	15	0.952	240	54	0.995	240	22	0.987	240	13	0.995
						260	31	0.998	260	16	0.995	260	8	0.985
						280	20	0.989	280	8	0.990	280	4.4	0.978
						298	9.2	0.970	298	4.1	0.974	298	3.3	0.976

§9. Details of quantum chemical calculations

9.1. Computational methodology

The methods of quantum theory of atoms in molecules (QTAIM)[11] and natural bond orbital (NBO) analysis[12] were used to analyze the electronic structure of the studied complexes, more specifically the nature and energy of the M–C and M–P bonds (M = Cu, Ag and Au). The QTAIM topological descriptors at the bond critical points (BCPs) were calculated using the Multiwfn program (version 3.2)[13] and the results of all-electron calculations using the scalar relativistic Douglas-Kroll-Hess Hamiltonian (DKH2)[14] and the B3LYP functional.[15] These calculations were performed for the XRD geometries of complexes **1**–**5** using the WTBS basis set[16] for Cu, Ag and Au and the DKH-def2-TZVP basis set[17] for all other atoms.

NBO analysis (for M–C and M–P coordination bonds, M = Cu, Ag, Au) was carried out using the NBO7 software package[18] and the GAUSSIAN16 software package.[19] In these calculations, each of complexes **1**–**5** was divided into 5 fragments: two cations (Cu$^+$, Ag$^+$ or Au$^+$) with a d^{10} valence shell, two carbene anions and a central ligand. Modified X-ray structures of the complexes were used, in which all phenyl groups of the central ligand were replaced by methyl groups. The orbital contributions to the M–C and M–P bond energies were calculated using second-order perturbation theory:

$$\Delta E_{DA}^{(2)} = n_D \langle \Phi_D | \hat{F} | \Phi_A \rangle^2 / (\varepsilon_D - \varepsilon_A),$$

where Φ_D and Φ_A as well as ε_D and ε_A are the natural Lewis-type orbitals of the donor (D) and acceptor (A) and their energies, respectively; n_D – the population of the natural orbital of the donor, and $\hat{F}$ – the Fock operator.

Positions of the maxima and oscillator strengths of electronic transitions in the electronic absorption spectra (EAS) of complexes **1**–**5** and their mononuclear fragments were calculated using time dependent density functional theory (TD-DFT)[20] using the hybrid B3LYP functional[15] and def2-TZVP basis set[21] (with ECP for Au). The Tamm-Dankoff approximation (TDA)[22] was not used in these calculations. We also carried out all-electron TD-DFT calculations with the scalar relativistic DKH2 Hamiltonian and the WTBS basis set for Au and the DKH-def2-TZVP basis set for all other atoms. The oscillator strengths for the $S_0 \rightarrow T_i$ electronic transitions were also calculated[23] using the QDPT approach[24] to calculate the mixing between singlet and triplet states. The corresponding XRD geometries of the complexes and their fragments were used in the calculations related to the EAS and photophysical properties in solid state.

The geometries of complexes **1**–**5** were also optimized at the B97-D3[25]/def2-TZVP (with ECP for Au) level in a methylene chloride and in acetonitrile; the solvent was taken into account via the CPCM model.[26] The ORCA 4.2.1 or 5.0.5 software packages[27] were used for all calculations. MOs were visualized in Chemcraft.[28]

9.2. The electronic structure of the complexes 1–5

The electronic structure and bonding interactions were analyzed for XRD geometries of complexes **1**–**5** using the QTAIM and NBO procedures. Table S3 shows that for complexes **1**–**3** the coordination bond lengths (both M–P and M–C, M = Cu, Ag) are close to or slightly shorter (up to ~0.1 Å) than the sum of the covalent radii of the corresponding atoms. In complexes **4** and **5**, only the Au–C bond lengths are close to the sum of covalent radii. In complex **4**, as mentioned above, the tetraphosphine ligand exhibit asymmetric coordination with a shorter distance close to the sum of covalent radii (2.43 Å) and an elongated distance reaching 2.8 Å in one of the chelate rings. In complex **5**, the asymmetry of the chelating rings grows and one of the Au–P distance is reaching 3.24 Å. Nevertheless, even in the latter case the

(3, −1) BCP was localized and a non-covalent bonding interaction ($|V_b|/G_b \sim 1$) between Au and P atoms was found with moderate energy (an orbital contribution is 13.6 kcal/mol, Table S3). The topological descriptor – the ratio $|V_b|/G_b$, is considered to be a good reliable indicator for classifying bonds: thus, covalent bonds are characterized by $|V_b|/G_b > 2$, bonding with $|V_b|/G_b < 1$ is non-covalent in nature, the bond in the intermediate case ($1 < |V_b|/G_b < 2$) was proposed to be considered partially covalent.[29]

Table S3. Experimental and calculated[a] coordination bond lengths (r_b, Å) in complexes **1–5**, sums of the covalent radii[30] of the bonded atoms (r_{cov}, Å), the QTAIM topological descriptors[11] (electron density (ρ_b), its Laplacian ($\Delta\rho_b$), and ratio of the potential V_b and kinetic G_b energy densities ($|V_b|/G_b$) at the bond critical points, (BCPs),[b] Mayer bond orders (P) and orbital (or CT) contributions ($|E_{CT}|$) to the bond energies, estimated using the NBO analysis and second-order perturbation theory.

	Bond	r_b XRD	r_b B97-D3	$\sum r_{cov}$	P	ρ_b	$\nabla^2\rho_b$	$|V_b|/G_b$	$|E_{CT}|$[c]$=\sum E^{(2)}$ kcal/mol	$E^{(2)}_{main}$, kcal/mol
1	Cu–P	2.30 ÷ 2.33	2.29 ÷ 2.33	2.39	0.27÷0.18	0.075 ÷ 0.077	0.17 ÷ 0.18	1.35 ÷ 1.36	57.1 ÷ 59.3	50.7 ÷ 52.7
	Cu–C	1.94, 1.96	1.93,1.95	2.05	0.21, 0.13	0.107	0.38	1.29	105.0±0.6	92.3±1.0
2	Ag–P	2.48 ÷ 2.54	2.46 ÷ 2.56	2.52	0.35÷0.28	0.060 ÷ 0.066	0.14 ÷ 0.15	1.27 ÷ 1.30	41.8 ÷ 46.3	35.9 ÷ 40.1
	Ag–C	2.11, 2.13	2.11, 2.12	2.18	0.41,0.32	0.094 ÷ 0.098	0.55 ÷ 0.34	1.24 ÷ 1.25	89.7, 91.2	77.2 ÷ 77.7
3	Ag–P	2.478	2.46 ÷ 2.58	2.52	0.28÷0.21	0.067	0.16	1.30	62.5 ÷ 68.6	51.9 ÷ 57.8
	Ag–C	2.097	2.10, 2.12	2.18	0.29	0.101	0.35	1.26	105.5	90.4
4	Au–P	2.27 ÷ 2.45 / 2.74[d]	2.31, 2.31 / 2.95, 2.98	2.43	0.57 / ~0.20[d]	0.079 ÷ 0.110 / 0.047[d]	0.16 ÷ 0.17 / 0.11[d]	1.37 ÷ 1.53 / 1.21[d]	81.4÷139.5 / 37.5	50.6÷92.4 / 25.4[d]
	Au–C	2.02 ÷ 2.11	2.05	2.09	0.28, 0.20	0.111 ÷ 0.117	0.35÷ 0.37	1.30 ÷ 1.31	~165.5	117.5 ÷ 122.3
5	Au–P	2.29 ÷ 2.59 / 3.24[d]	2.31, 2.30 / 2.92, 3.03	2.43	0.57÷0.20 / <0.1[d]	0.060 ÷ 0.108 / 0.020[d]	0.13 ÷ 0.18 / 0.04[d]	1.28 ÷ 1.51 / 1.04[d]	184.5 ÷ 54.6 / 13.6[d]	38.2 ÷ 137.1 / 8.8[d]
	Au–C	1.99 ÷ 2.03	2.05	2.09	0.28, 012	0.130 ÷ 0.140	0.41÷ 0.42	1.34 ÷ 1.37	230.3,193.1	133.6 ÷ 161.5

[a] Geometry optimization was performed at the B97-D3/def2-TZVP (with ECP for Au) level. [b] Based on the gas-phase DKH2-B3LYP calculations at XRD geometry; ρ_b and $\Delta\rho_b$ are given in a.u., that is, e/a_0^3 and e/a_0^5, respectively. [c] In the NBO analysis, every contribution is evaluated using the second-order perturbation theory as $\Delta E^{(2)} = \left(n_D\langle\Phi_D|\hat{F}|\Phi_A\rangle^2\right)/(\varepsilon_D - \varepsilon_A)$, where Φ_D and Φ_A, and ε_D and ε_D are the localized orbitals of D and A and their energies, respectively; n_D is the occupation number of the donor localized orbital, and $\hat{F}$ is a Fock operator. [d] Data corresponding to bonding interactions of Au and P atoms, the distance between which are much greater than $\sum r_{cov}$.

The QTAIM topological analysis shows that all coordination bonds (M−P and M−C) with the lengths smaller or slightly longer than $\sum r_{cov}$ are characterized by moderate electron densities (0.06−0.14), rather large and positive values of their Laplacian (0.34–0.55), and negative electronic energy densities at the BCPs. These values are characteristic of donor−acceptor bonds involving M^I centers with an apparent closed-shell. Moreover, for each complex the ρ values at BCP for M–C bonds are significantly higher than for M–P bonds, indicating the higher energies of the former. According to the NBO analysis, the orbital contribution to the bond energy is also significantly higher for M–C (M = Cu, Ag, Au) bonds compared to M–P.

At the same time, the predominant contribution to the bond energy ($E^{(2)}_{main}$) in all cases is due to the interaction of a lone pair of P or C atoms (donor) with the ns orbital (n = 4 for Cu, 5 for Ag, and 6 for Au) on the M^I cation (acceptor) (Figure S27). As for M–C bonds, the orbital contribution is much higher for Au–C bonds than for Cu–C and Ag–C, for which they are close. If we exclude Au–P bonds with length much greater than the sum of r_{cov}, Au–P bonds appear to be much stronger than Cu–P and Ag–P, which are close in energy. It is known that the relativistic nature of the Au atom is responsible for the fact that the bond energy of Au–L is significantly higher than Ag–L, where L is any ligand.[31]
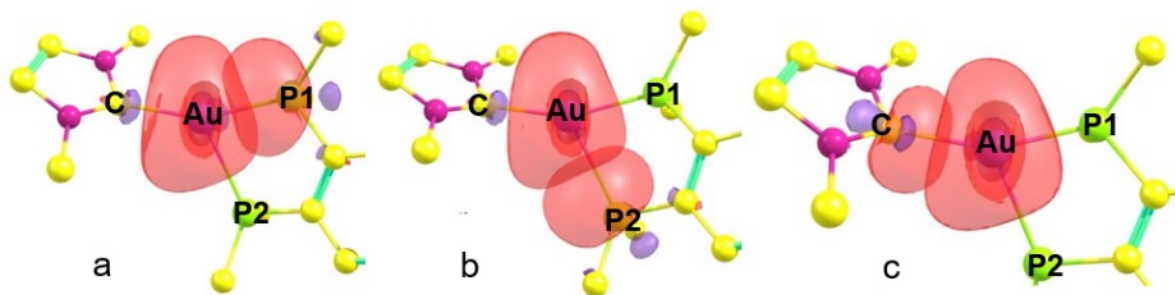
Figure S27. Fragment of the structure of complex **4** with natural orbitals (lone pairs, lp, of phosphorus and carbon atoms, as well as the 6s orbital of Au), whose interactions give the predominant orbital contributions to the Au–P (a and b) and Au–C (c) bonds: a) lp(P1) → 6s(Au), b) lp(P2) → 6s(Au), and c) lp(C) → 6s(Au).

In addition, the geometry of complexes **1**−**5** was optimized at the B97-D3/def2-TZVP level in methylene chloride. It can be seen (Table S3) that in complexes **1**–**3** the lengths of the optimized M–C bonds are close to those in the crystal structure. At the same time, in both complexes **4** and **5**, the optimization leads to the alignment of Au–C bonds. It should be noted that in general, after optimization, the geometry of complexes **4** and **5** becomes more symmetric, namely with one short (2.31 Å) and one long (2.97±0.06 Å) Au–P bond around each Au cation. At the same time, even the longest Au–P bonds (3.03 Å in the optimized and 3.23 Å in the XRD structures of **5**) are still much shorter than the sum of the VdW radii (4.12 Å[32]), which is consistent with the results of QTAIM and NBO analysis (Table S3).

Note that the electronic energies of the optimized *trans*-type complexes (**3** and **5**) are predicted to be lower than that of the *cis*-type complexes (**2** and **4**): the energy difference is very small (0.3 kcal/mol) for Ag(I) complexes, but much higher (7.7 kcal/mol) for Au complexes.

9.3. Electronic absorption spectra. Experiment and TD-DFT calculations.

In this work, two types of experimental electronic absorption spectra (EAS) were analyzed: EASs recorded in solution and EASs in the solid state as a Kubelka-Munk function[6]. Figure S28 shows that the EAS of the investigated complexes in solution are very similar, characterized by a very intense UV band with a maximum at 232 nm (~43100 cm^{-1}) and a much less intense long-wavelength band in the near-UV and visible region with maxima between 370 and 390 nm. The electronic absorption spectra in the solid state (K-M functions) agree well with the solution spectra, although the absorption bands in the solid state are noticeably broader and their maxima are slightly shifted to the red region. Thus, to interpret the EAS, we can perform calculations for individual molecules in a gas or in solution.
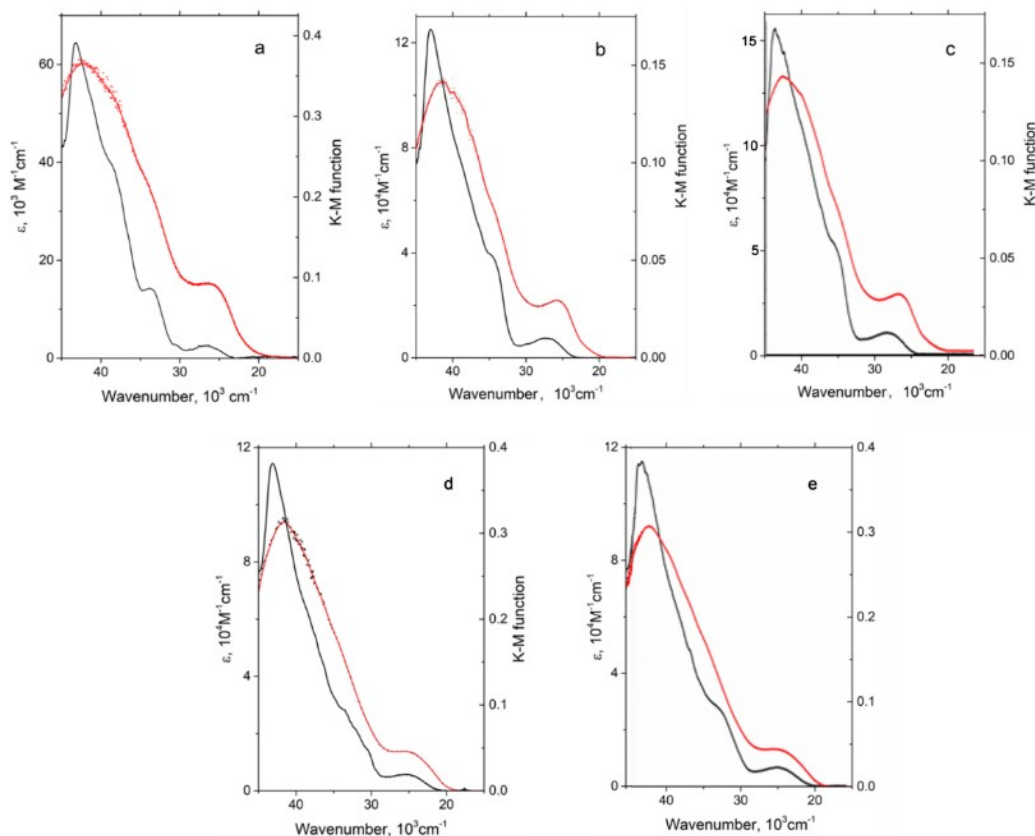
Figure S28. Electronic absorption spectra in CH_2Cl_2 solution (black) and Kubelka-Munk functions (red) for mixtures of $BaSO_4$ powder with ~0.05 mol% of complexes **1** (a), **2** (b), **3** (c), **4** (d) and **5** (e).

Figure S29 shows the near-UV and visible spectral region of complex **1** in acetonitrile solution together with the results of TD-DFT calculations. These calculations were performed taking into account the CH_3CN solvent and for the structure optimized in the same solvent. It can be seen that the calculations agree quite well with the experimental spectrum. It should be noted that four transitions to the excited states $S_1 - S_4$ contribute to the long-wavelength band with a maximum at 26800 cm^{-1} (373 nm).

Figure S29. Experimental EAS in CH_3CN (black) and calculated at the TD-B3LYP/def2-TZVP level positions and oscillator strengths (f, right axis) of the electronic transitions (blue bars) for complex **1**.

Figure S30. (a) Experimental solid-state EAS as a Kubelka-Munk function (black curve) and calculated at the TD-B3LYP/def2-TZVP level positions and oscillator str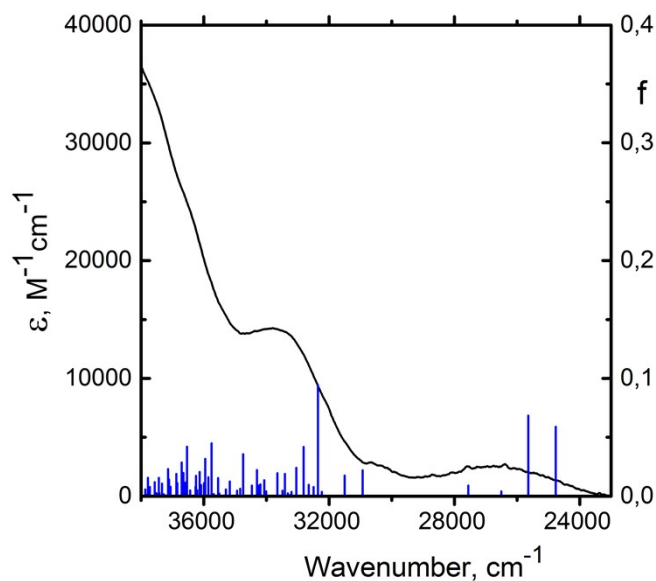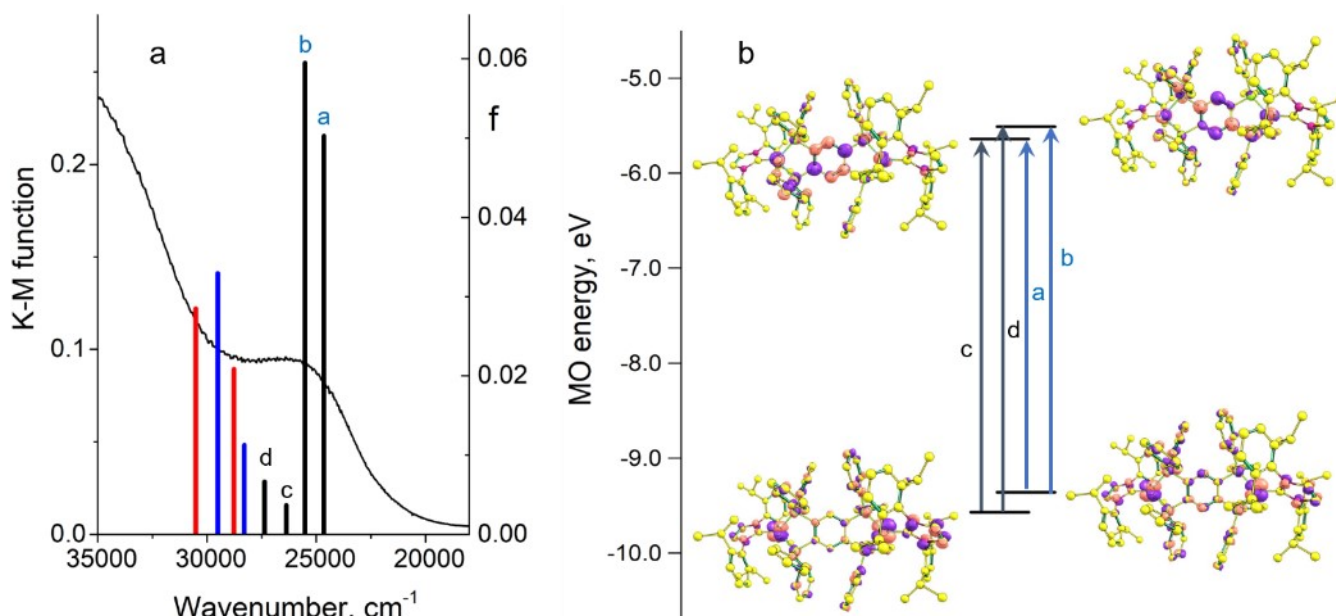engths (f, right axis) of electronic transitions for complex **1** (black bars) and for the left (blue bars) and right (red bars) fragments of **1** (Scheme1). (b) The electron transitions (a – d) and corresponding molecular orbitals (HOMO, HOMO-1 and LUMO, LUMO+1) that dominate the long-wavelength electronic excitations of complex **1**.

Let us consider these long-wavelength transitions in more details, based on similar calculations for the XRD structure of **1** (Fig. S30). Figure S30a demonstrates even better agreement between the solid-state spectrum and the calculations compared to the solution spectrum (Fig. S29). Note that the wave-function of each of the lower excited states ($S_1 – S_4$) is dominated by a single determinant (88 – 95%), which facilitates the interpretation of the spectrum. These determinants correspond to electron promotions from one of the two molecular orbitals that are close in energy, HOMO or HOMO-1 ($\Delta E = 0.21$ eV), to LUMO or LUMO+1, which are also very close in energy ($\Delta E = 0.13$ eV). The energetic proximity of the corresponding MO pairs leads to the proximity of the transition energies, resulting in the overlap of the absorption bands of the corresponding excitations and, consequently, to the formation of a single absorption band in the EAS. Note that the main contributions to HOMO and HOMO-1 give the difference and sum of the d-AOs of Cu cations. The LUMO and LUMO+1 are localized mainly on the bridging ligand and the main contributions come from the π^*-MOs of benzene ring. Thus, all these transitions are of the MLCT type.

Table S4. Energies (ν) and oscillator strengths (f) for transitions to the four lower excited singlet states, calculated at the TD-B3LYP/def2-TZVP level (with ECP for Ag and Au), and the calculated energy difference between the lower singlet and triplet states for complexes **1**–**5**, as well as maxima of experimental long-wavelength bands in solid-state EAS and extinction coefficient in CH_2Cl_2 solutions of complexes **1**, **2** and **4**.

Complex	**1**		**2**		**3**		**4**		**5**	
Transition	ν, cm^{-1}	f[a]	ν, cm^{-1}	f[a]	ν, cm^{-1}	f[a]	ν, cm^{-1}	f[a]	ν, cm^{-1}	f[a]
$S_0 \rightarrow S_1$	24650	0.050	25135	0.099	23942	0.181	22749	0.118	20674	0.064
$S_0 \rightarrow S_2$	25515	0.060	25723	0.088	26173	0.004	23446	0.054	23919	0.018
$S_0 \rightarrow S_3$	26372	0.004	26981	0.002	26613	0	23655	0.001	26374	0.006
$S_0 \rightarrow S_4$	27365	0.007	27342	0.005	28293	0	24360	0.002	28856	0.000
ν_{max}^{exp}, cm^{-1}	26390 (379 nm)		26300 (380 nm)		–		25580 (391 nm)		–	
ε_{max}^{exp}, M^{-1}cm^{-1}, $\sum f_i$	2.6×10^3, 0.121		7.3×10^3, 0.194		–		5.6×10^3, 0.175		–	
$S_0 \rightarrow T_1$	23438	No	23670	No	22481	No	21550	No	19860	No
$S_0 \rightarrow T_2$	24170	No	23806	No	24455	No	21972	No	22793	No
$S_0 \rightarrow T_3$	25316	No	24808	No	24839	No	22288	No	23676	No
$S_0 \rightarrow T_4$	25892	No	24933	No	26790	No	23262	No	24918	No
ΔE_{ST}, cm^{-1}	1212		1465		1461		1199		814	

[a]Oscillator strengths are calculated through the matrix element of transition dipole moment.

TD-DFT calculations were also carried out for complexes **2**–**5**, and the results obtained demonstrate good agreement with experiment for the entire series of complexes (**1**–**5**). In fact, we performed two types of calculations that gave similar results. The first calculations are non-relativistic with basis sets with ECP for Ag and Au (Table S4). In the second type of calculations, scalar-relativistic effects were taken into account using the DKH2 Hamiltonian and the all-electron basis sets; the QDPT procedure was used to calculate the energy splitting of triplet states and oscillator strengths for the $S_0 \rightarrow T_i$ transitions (see Section 9.1).

Table S4 summarizes the results obtained for complexes **1**–**5** using non-relativistic Hamiltonian. Note that, as in the case of complex **1**, for **2**–**5**, the wave-functions of the lower excited states ($S_1 - S_4$) are dominated by a single determinant corresponding to electron promotions from HOMO or HOMO-1 to LUMO or LUMO+1, and the appearance of these MOs qualitatively the same as that of complex **1** (Fig. S30b). Thus, the above interpretation of the long-wavelength absorption band applies to the entire series of complexes **1**–**5**, including the assignment of the four lowest energy transitions to the MLCT type. It should be noted that for all complexes, the oscillator strengths (f) of the long-wavelength transitions (a) exceed the f values of the other transitions, two of which are very low.

Table S5. The energies (ν) and oscillator strengths (f) for transitions to the four lower excited singlet and triplet states calculated at the time dependent DKH2-B3LYP/DKH-def2-TZVP level (full-electron WTBS basis set for Cu, Ag and Au), radiative rate constants for lowest singlet and triplet states calculated using formula (2), and the energy difference between the lowest singlet and triplet states of complexes **1–5**.

Complex	1		2		3		4		5	
Transitions	ν, cm^{-1}	f^a	ν, cm^{-1}	f^a	ν, cm^{-1}	f^a	ν, cm^{-1}	f^a	ν, cm^{-1}	f^a
$S_0 \rightarrow S_1$	25186	0.060	25882	0.086	24701	0.177	24337	0.117	21932	0.077
$k_{rad}^{S,calc}$, s^{-1}	2.85×10^7		4.31×10^7		8.08×10^7		5.18×10^7		2.77×10^7	
$S_0 \rightarrow S_2$	26172	0.050	26476	0.097	27041	0.004	24799	0.049	24711	0.016
$S_0 \rightarrow S_3$	27134	0.005	27759	0.003	27508	0.000	25134	0.004	27623	0.007
$S_0 \rightarrow S_4$	28146	0.006	28219	0.004	29328	0.000	25639	0.001	29301	0.000
$S_0 \rightarrow T_1$	23952	$3.7\cdot10^{-6}$	24148	$3.3\cdot10^{-6}$	23166	$1.2\cdot10^{-7}$	23041	$1.8\cdot10^{-5}$	20995	$3.0\cdot10^{-5}$
$k_{rad}^{T,calc}$, s^{-1}	1.59×10^3		1.44×10^3		48.2		7.15×10^3		9.89×10^3	
$S_0 \rightarrow T_2$	24605	$8.0\cdot10^{-6}$	24486	$8.4\cdot10^{-7}$	25063	$7.7\cdot10^{-4}$	23268	$2.6\cdot10^{-5}$	23426	$4.3\cdot10^{-5}$
$S_0 \rightarrow T_3$	26078	$4.6\cdot10^{-5}$	24898	$2.3\cdot10^{-7}$	25709	0.000	23668	$1.3\cdot10^{-4}$	23736	$3.6\cdot10^{-5}$
$S_0 \rightarrow T_4$	26597	$1.7\cdot10^{-5}$	24996	$1.5\cdot10^{-6}$	27610	0.000	24424	$6.3\cdot10^{-3}$	25373	$9.8\cdot10^{-6}$
ΔE_{ST}, cm^{-1}	1234		1734		1531		1296		937	

^{a} Oscillator strengths are calculated through the matrix element of transition dipole moment; for the $S_0 \rightarrow T_i$ transitions, these matrix elements were calculated taking into account spin-orbit coupling.[22]

Table S5 shows that the results of all-electron calculations with the scalar relativistic Hamiltonian are similar to those obtained in calculations with the non-relativistic Hamiltonian and ECP. However, in the first case, f values for $S_0 \rightarrow T_i$ transitions were also obtained. For complexes **1–3**, the oscillator strengths for $S_0 \rightarrow T_i$ transitions are about 5-6 orders of magnitude lower than for $S_0 \rightarrow S_i$. For complexes **4** and **5**, this difference is much smaller. At the same time, for the $S_0 \rightarrow T_1$ transitions, the difference in f between complexes **1–3** and Au complexes (**4, 5**) is about one order of magnitude, which correlates with the difference in their phosphorescence times (~130 μs for **4** and **5** and 1.7–3 ms for **1–3**). Thus, the calculations are in semi-quantitatively agreement with the experiment. In addition, we have estimated radiative rate constants for the first excited singlet and triplet states using the calculated values of f and formula (2).

The pseudo-symmetrical dinuclear complexes **1–5** were designed based on the idea of Yersin et al.[33] proposed by analogy with the Davydov model for molecular crystals[34] **Scheme S1** shows the chemical structure of the dinuclear complex and its left and right fragments obtained by replacing one of the $M(NHC)(PPh_2)_2$ fragments with two H atoms. The symmetry-based design strategy was based on the assumption of high symmetry of dinuclear complexes and, consequently, collinearity of the transition dipole moments of the left and right mononuclear fragments. Based on this assumption, the transition dipole moments (TDMs, μ_{0i}) of the left and right fragments were expected to add and subtract, giving double and zero TDMs of the dinuclear system. The oscillator strength is described by the equation[35]

$$f_{0\rightarrow i} = \frac{2m_e}{3\hbar e^2}\omega_{0i}|\mu_{0i}|^2 ,$$

(1)

so a fourfold increase in the oscillator strength of the dinuclear complex compared to the mononuclear one is to be expected. In turn, the radiative rate constant for the excited state is proportional to the oscillator strength[35]

$$k_{rad}(s^{-1}) = 2\frac{g_{s0}e^2\omega_{i0}^2}{g_{s1}c^3m_e}f_{0\to i} = 0.748cm^2(\Delta E)^2 \times f_{0\to i}$$

(2)

and its fourfold increase is also anticipated.

However, in the solid state, complexes **1**–**5** exist as *cis*- or *trans*-isomers. The same structures are predicted for them in solution (end of Section 9.2). To better understand the applicability of the symmetry-based strategy[33] to our complexes, we have also performed calculations of the spectroscopic properties of mononuclear complexes (left and right).
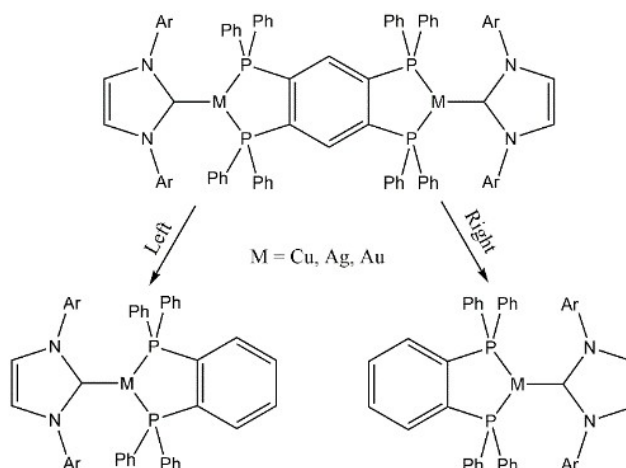
Scheme S1. Chemical structure of complexes **1**–**5** and their left and right fragments.
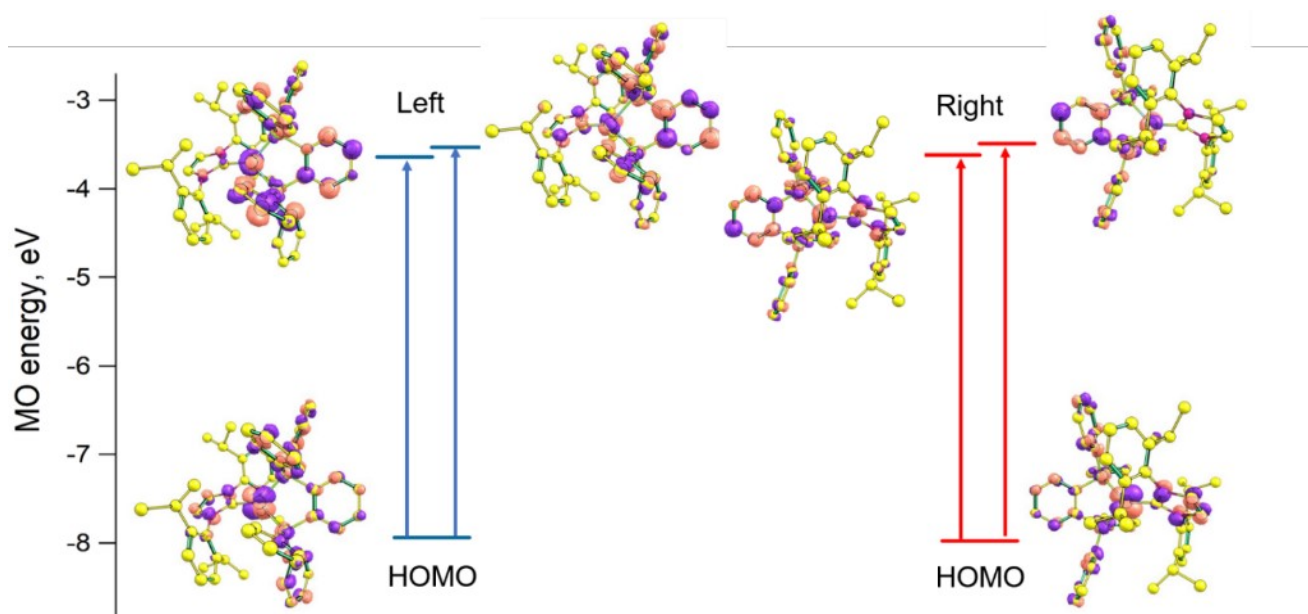

Figure S31. Electronic transitions between the corresponding molecular orbitals (HOMO and LUMO, LUMO+1) calculated at the TD-B3LYP/def2-TZVP level, which dominate the long-wavelength electronic excitations (S$_0$ → S$_1$, S$_0$ → S$_2$) of the left and right fragments of complex **1** (see Fig. S17a for the positions and oscillator strengths of these transitions).

As an example, Figure 30a shows the positions and oscillator strengths of long-wavelength transitions not only for complex **1**, but also for its left (blue bars) and right (red bars) fragments. Similar to the complexes **1**–**5**, the wave-functions of the S$_1$ and S$_2$ excited states of their left and right fragments are dominated by a single determinant (>95%). These determinants correspond to electron promotions from the HOMO to LUMO or LUMO+1, which are close in

energy (Fig. S31). The energetic proximity of the two transitions is due to the close energy of LUMO and LUMO+1, which are largely localized on the benzene ring of the ligand.

Figure S32a displays the transition dipole moments (TDMs) for the electronic excitations of complex **1** and its left and right fragments. Since the symmetry of complex **1** (as well as **2–5**) is very low (Fig. S32a), the TDMs (μ_{0i}) of the left and right fragments (L and R) are very far from collinearity, so it is very difficult to find a simple relationship between the TDMs of the fragments and complex **1** (same for **2–5**). We tried to find this relationship using difference density plots (DDP). As an example, Figures S32b-d show the DDPs for certain transitions of the left and right fragments and the DDP for the long-wavelength transition ($S_1 \rightarrow S_0$) of **1**. The left and right fragment transitions were chosen so that their sum resembles the DDP for $S_1 \rightarrow S_0$ transition of the whole molecule **1**. However, as can be seen in Figure 19d, the transition dipole moment (TDM μ_{01}) is not equal to the sum of the TDMs of fragments. Nevertheless, the TDMs of the first and second transitions (in S_1 and S_2 states of **1**) are much larger than the TDMs of the mononuclear complexes, which provides approximately 2–3 times greater oscillator strength of the long-wavelength transitions in **1** compared to its left and right fragments. A similar situation is observed for the other complexes (**2–5**). Thus, the Davydov model does not work for dinuclear complexes **1–5** quantitatively, although a significant increase in dipole moment and oscillator strength, and hence radiative constant, compared to mononuclear complexes does occur.
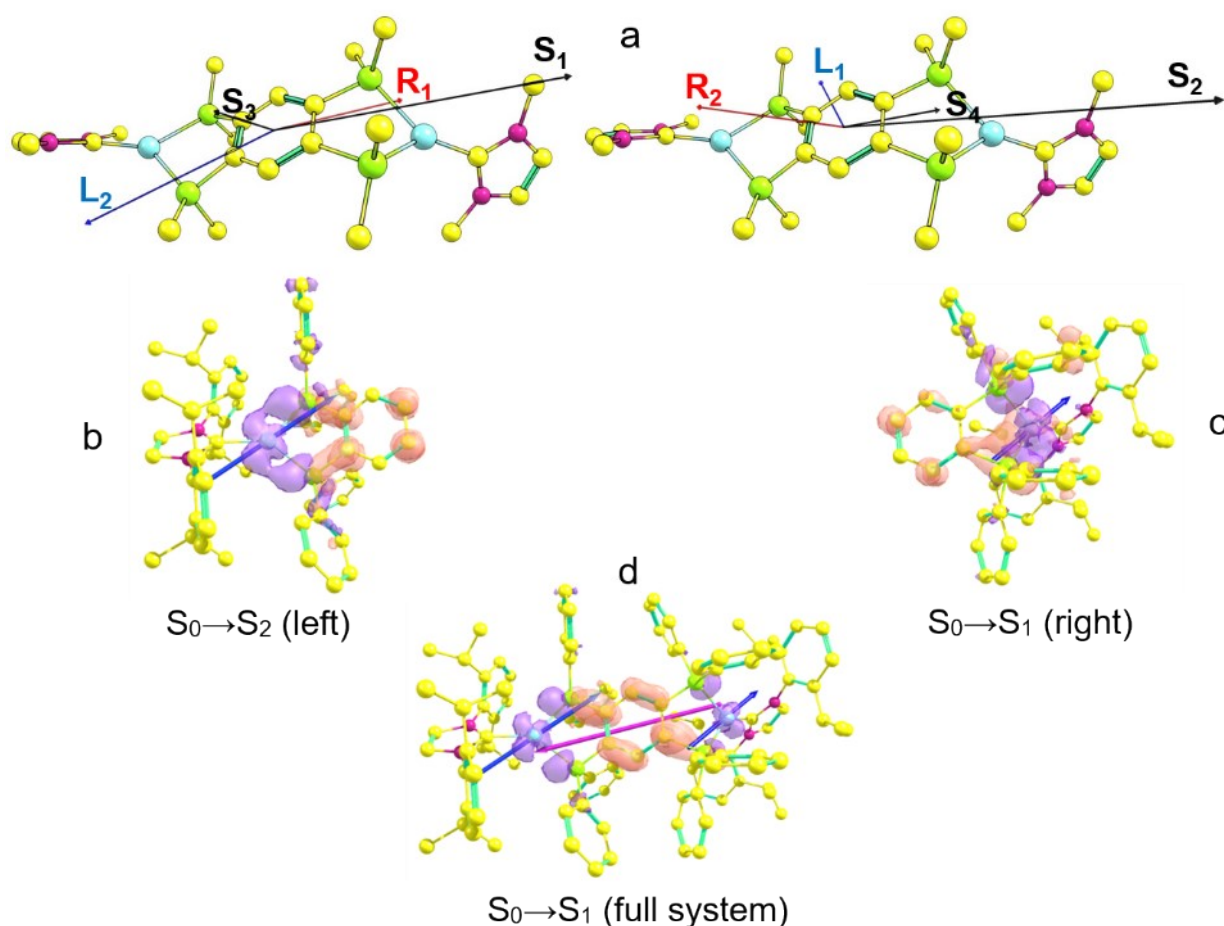

Figure S32. (a) Structure of complex **1** and transition dipole moments (TDMs) for the four long-wavelength excitations (S_1 - S_4) of this complex (black vectors) and TDMs for the two excitations of the left (blue, L_1, L_2) and right (red, R_1, R_2) mononuclear fragments. (b) Left fragment with difference density and TDM for the $S_0 \rightarrow S_2$ transition. (c) Right fragment with difference density and TDM for the $S_0 \rightarrow S_1$ transition. (d) Molecule **1** with difference density and TDM for the $S_0 \rightarrow S_1$ transition (magenta vector), and TDMs for the left and right fragments (blue vectors). All difference

densities are represented as isosurfaces with a density of 0.002 a.u. Calculations were performed at the TD-B3LYP/def2-TZVP level.

§10. Photophysical data

10.1. Computational results and analysis of the photophysical models

The kinetics of *temperature dependent delayed fluorescence* (TADF) is typically analyzed within the simple three level model presented in Figure S33. Figure S33 shows the channels of radiative (k_{rad}) and non-radiative (k_{nr}) energy relaxation as well as the intersystem crossing between S_1 and T_1 excited states (k_{soc}^+, k_{soc}^-). The evolution of singlet and triplet excited states can be described by the system of kinetic equations (3):

$$\begin{pmatrix} S_1 \\ T_1 \end{pmatrix} = \begin{pmatrix} -k_{S1 \to S0} - k_{soc}^+ & k_{soc}^- \\ k_{soc}^+ & -k_{T1 \to S0} - k_{soc}^- \end{pmatrix} \begin{pmatrix} S_1 \\ T_1 \end{pmatrix}. \tag{3}$$

This system has an analytical solution, although rather cumbersome, in the form of linear combinations of two exponential functions with characteristic times $\dfrac{1}{|\lambda_1|}$ and $\dfrac{1}{|\lambda_2|}$; the values $\lambda_{1,2}$ are functions of the rate constants presented in eq. 3.
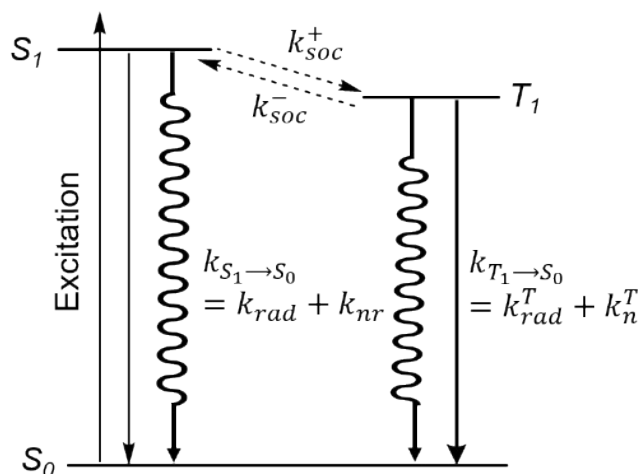

Figure S33. Energy diagram with the ground (S_0) and two excited (S_1 and T_1) states involved in the TADF process.

For molecules exhibiting TADF, the equilibrium of the S_1 and T_1 states should occur much faster than their decay. Assuming also very close electronic structures of S_1 and T_1, the equilibrium constant has the form (4):

$$K = \frac{k_+^{SOC}}{k_-^{SOC}} \approx 3\exp\left(\frac{\varepsilon_{S1} - \varepsilon_{T1}}{k_B T}\right) = 3\exp\left(\frac{\Delta E_{ST}}{k_B T}\right). \tag{4}$$

Taking into account the above assumptions, the time of photoluminescence (τ) will take the form (5) [36]:

$$\tau = \frac{3 + exp\left(-\dfrac{\Delta E_{ST}}{k_B T}\right)}{3k_{T1 \to S0} + k_{S1 \to S0} \times exp\left(\dfrac{-\Delta E_{ST}}{k_B T}\right)} = \frac{1 + \dfrac{1}{K}}{k_{T1 \to S0} + \dfrac{k_{S1 \to S0}}{K}}. \tag{5}$$

Under the assumption of fast equilibration, analytical solutions can be replaced by asymptotical:

$$S_1 \approx S_1^0 \cdot \frac{1}{K+1} \cdot \exp\left(-|\lambda_1| \cdot t\right), \tag{6}$$

$$T_1 \approx S_1^0 \cdot \frac{K}{K+1} \cdot \exp\left(-|\lambda_1| \cdot t\right)$$

(7)

$$|\lambda_1| \approx k_{S1 \to S0} \times \frac{1}{K+1} + k_{T1 \to S0} \times \frac{K}{K+1}.$$

(8)

The quantum yield (*PLQY*), in turn, is expressed as follows

$$PLQY \approx \frac{k_{rad} \times \frac{1}{K+1} + k_{rad}^T \times \frac{K}{K+1}}{|\lambda_1|} = \frac{k_{rad}^T + \frac{k_{rad}}{K}}{k_{T1 \to S0} + \frac{k_{S1 \to S0}}{K}} = \frac{k_{rad} + K \times k_{rad}^T}{k_{S1 \to S0} + K \times k_{T1 \to S0}}.$$

(9)

$$\tau \approx \frac{1}{k_{T1 \to S0} + \frac{k_{S1 \to S0}}{K}}.$$

If $K \gg 1$,

(10)

If also $K \times k_{rad}^T \ll k_{rad}$, then

$$PLQY \approx \frac{k_{rad}}{K} \times \tau.$$

(11)

Thus, the radiative rate constant can be estimated using eq. (12);

$$k_{rad} \approx K \times PLQY/\tau.$$

(12)

Unfortunately, the assumption ($K \times k_{rad}^T \ll k_{rad}$) used to calculate k_{rad} (12) is too strict and corresponds to a negligible contribution of phosphorescence to the total luminescence intensity. If we do not use this assumption, then

$$PLQY \approx (\frac{k_{rad}}{K} + k_{rad}^T) \times \tau.$$

(13)

To calculate k_{rad} from (13), we will propose that

$$k_{rad}^T = 1/\tau(77\ K).$$

(14)

Thus, two types of calculations of k_{rad} will give both the under- and overestimated values.

We can also calculate the ration of the fluorescence (I(S_1)) to phosphorescence (I(T_1)) intensity, which is described by the expression

$$I(S_1)/I(T_1) = \frac{N(S_1) \times k_{rad}}{N(T_1) \times k_{rad}^T},$$

(15)

where $\frac{N(T_1)}{N(S_1)} = K$. Thus,

$$I(S_1)/I(T_1) = \frac{k_{rad}}{K \times k_{rad}^T}.$$

(16)

In turn, the contribution of fluorescence to the total intensity (I_0) of luminescence is described by the formula

$$\frac{I(S_1)}{I_0} = 1/(1 + \frac{K \times k_{rad}^T}{k_{rad}}).$$

(17)

Contribution of phosphorescence is equal to

$$\frac{I(S_1)}{I_0} = \frac{K \times k_{rad}^T}{k_{rad}} \bigg/ \left(1 + \frac{K \times k_{rad}^T}{k_{rad}}\right) \tag{18}$$

10.2. Experimental data and their analysis

The temperature dependences of τ for complexes **1**–**5** were approximated using formula (5) corresponding to the 3-level model (Fig. S33), assuming a very close electronic structure of the S_1 and T_1 states and rapid establishment of equilibrium between them. Figure S34 displays the experimental temperature dependences of τ and their approximations for all studied complexes. The best-fit parameters for **1**–**5** are summarized in Table S6. Figure S34 shows that experiment and approximation agree very well in the case of complexes **1** and **2**, for complex **3** the agreement is noticeably worse. We failed to satisfactorily approximate the temperature dependences of τ for Au complexes **4** and **5**; in these cases, systematic deviations of the high-temperature experimental values from the fit are clearly visible (Fig. S34d,e).
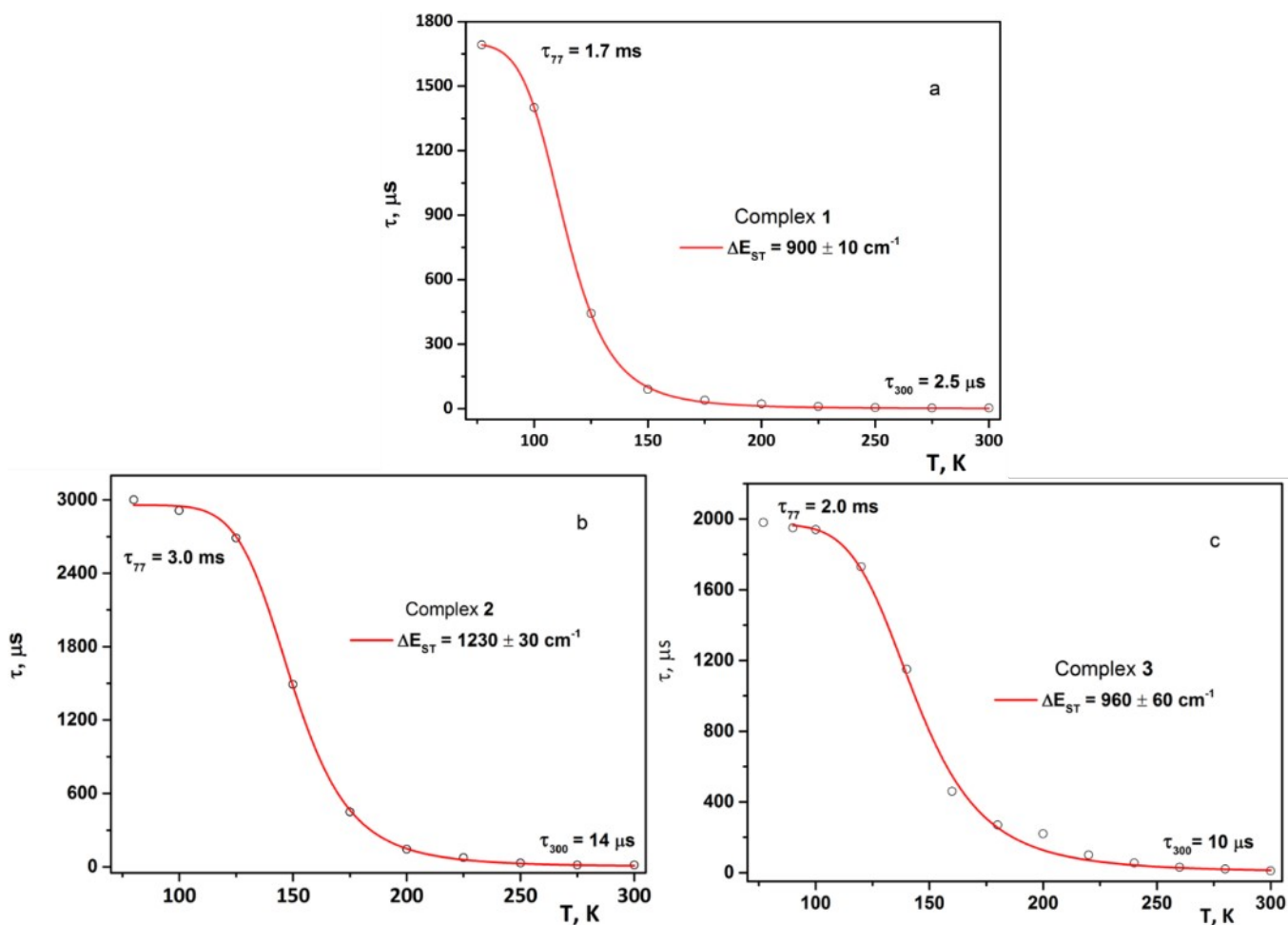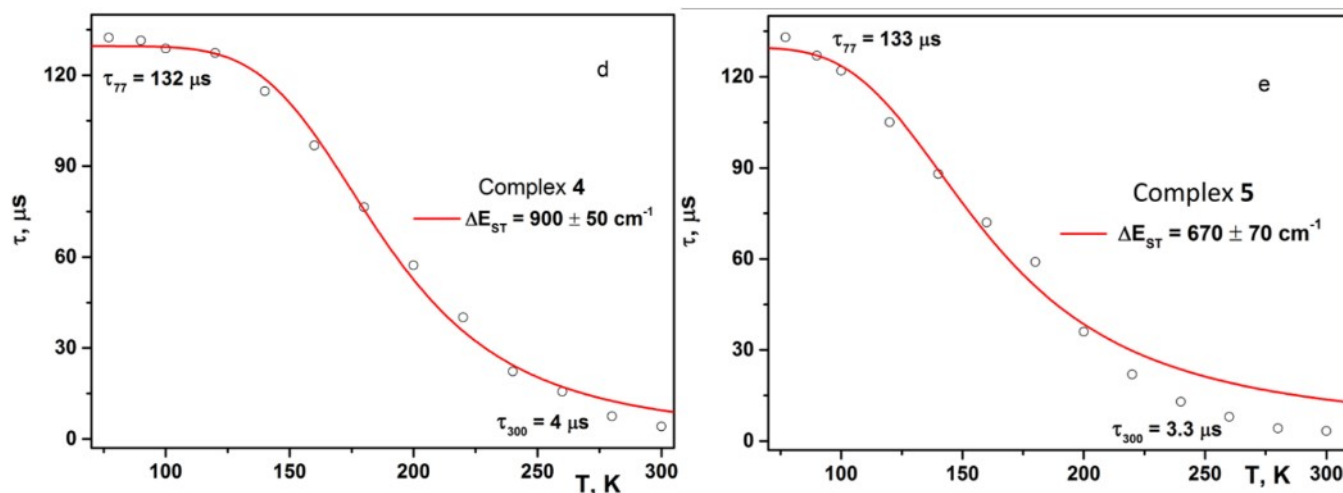
Figure S34. Experimental temperature dependences of the photoluminescence time (τ) for complexes **1**–**5** (open black circles) and their best fitting using equation (5).

Table S6. The best-fit parameters obtained for complexes **1**–**5** by approximating the temperature dependence of τ using formula (5); the equilibrium constant at 298 K was calculated using the best-fit ΔE_{ST} value.

Best-fit parameters	1	2	3	4	5
$k_{T1 \to S0}$, s^{-1}	$(5.88\pm0.02)\times10^2$	$(3.38\pm0.02)\times10^2$	$(5.06\pm0.07)\times10^2$	$(7.7\pm0.1)\times10^3$	$(7.9\pm0.2)\times10^3$
$k_{S1 \to S0}$, s^{-1}	$(1.6\pm0.3)\times10^8$	$(1.3\pm0.5)\times10^8$	$(1.9\pm1.1)\times10^7$	$(2.3\pm0.9)\times10^7$	$(8.8\pm5.2)\times10^6$
ΔE_{ST}, cm^{-1}	900 ± 10	1230 ± 40	940 ± 60	900 ± 60	680 ± 70
$K = 3 \cdot \exp\left(\dfrac{\Delta E_{ST}}{k_B T}\right)$	232 ± 11	1140 ± 240	280 ± 90	230 ± 80	80 ± 30

Using the best-fit parameters (Table S6) and experimental values of absolute quantum yields and value of τ at 298 K, the radiative rate constants for S$_1$ states ($k^{S, exp}_{rad}$) were estimated applying formula (12) (row, designated as 1 in Table S6) or formulas (13) and (14) (row, designated as 2 in Table S7). Table S7 is also supplemented with the values of radiative rate constants calculated from results of relativistic TD-DFT calculations (k^{calc}_{rad}, $k^{T, calc}_{rad}$). It can be seen that the difference between the radiative rate constants predicted on the basis of DFT calculations (k^{calc}_{rad}) and those estimated from experimental data and fitting parameters (k^{exp}_{rad}) reaches 2–3 times. The values of $k^{T, calc}_{rad}$ are overestimated significantly for **1**–**3** and are more reasonable for the Au complexes **4** and **5**.

Table S7. Experimental values of quantum yields and PL lifetimes at 298 K and 77 K, as well as radiative rate constants (k_{rad}^{exp}) evaluated using formula (12) or (16 and (17),) and calculated using results of TD-DFT calculations (k_{rad}^{calc}, $k_{rad}^{T,calc}$) for the lowest excited singlet and triplet states of complexes **1**–**5** estimated.

		1	**2**	**3**	**4**	**5**
$PLQY$(298 K)		0.85	0.57	0.89	0.87	0.58
τ(298 K), s		2.5×10^{-6}	15×10^{-6}	9.2×10^{-6}	4.1×10^{-6}	3.5×10^{-6}
k_{rad}^{exp}, s^{-1}	77–300 K (1)	7.9×10^{7}	4.3×10^{7}	2.7×10^{7}	4.9×10^{7}	1.3×10^{7}
	77-300 K (2)	7.85×10^{7}	4.26×10^{7}	2.69×10^{7}	4.7×10^{7}	1.24×10^{7}
	200–300 K	–	–	1.1×10^{8}	4.0×10^{8}	1.5×10^{8}
k_{rad}^{calc}, s^{-1}		2.9×10^{7}	4.3×10^{7}	8.1×10^{7}	5.2×10^{7}	2.8×10^{7}
τ(77 K), s		1.69×10^{-3}	3.00×10^{-3}	1.98×10^{-3}	1.32×10^{-4}	1.33×10^{-4}
$1/\tau$(77 K), s^{-1}		$5{,}92\times10^{2}$	3.33×10^{2}	$5{,}05\times10^{2}$	7.58×10^{3}	7.52×10^{3}
$k_{rad}^{T, calc}$, s^{-1}		1.6×10^{3}	1.4×10^{3}	48.2	7.2×10^{3}	9.9×10^{3}
$I(T_1)/I_0\times100$, %		0.2	0.9	0.53	3.6	4.7

Table S7 shows that the use of formulas (13), (14) changes the values of k_{rad}^{exp} negligibly, namely by less than 1% for **1**–**3**, and by about 4% for the Au complexes **4** and **5**. Using results of Table S7, obtained with the three level model, we estimated the contribution of phosphorescence in the total quantum yield of luminescence using (formulas (16) – (18)). The contribution of phosphorescence to the total luminescence quantum yield was estimated to be very small: less that 1% for compounds **1**–**3**, and about 4% for the Au complexes **4** and **5**.

Four-level model. As mentioned above, for compounds **1**–**5**, the four lowest singlet excited states are close in energy, and the same is true for the lowest triplet states. Thus, in principle, the failure to describe the temperature dependences of τ using equation (5) may be due to the participation of more than two excited states in the equilibrium. The results of calculations show that this is possible (Tables S4, S5). Unfortunately, the calculations predict the energies of the Franck-Condon states, not the relaxed states or minima at the PES. Data of Tables S4, S5 show that situations with one, two, or even three triplet states below S_1 are possible, but there is no correlation between the number of such triplets and the quality of the approximation using the equation (5). However, we found it useful and even necessary to consider a four-level model with two excited triplet states involved in TADF (Fig. S35).
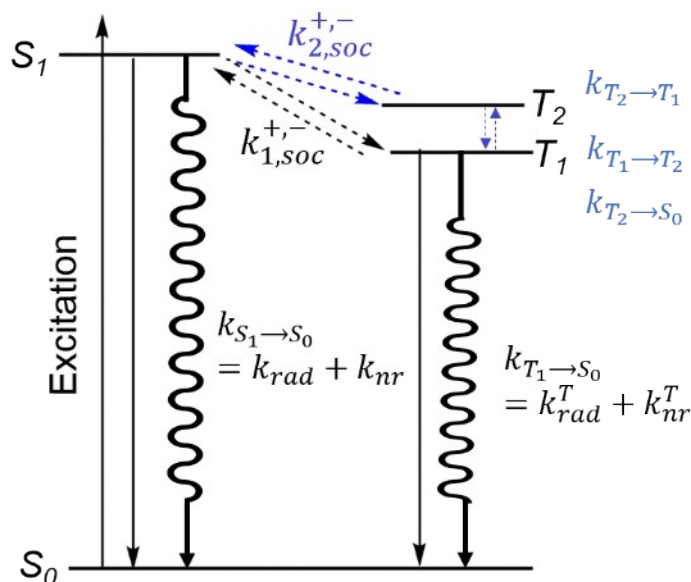
Figure S35. Energy diagram with the ground (S_0) and three excited (S_1, T_1 and T_2) states involved in the TADF process.

The system of three linear differential equations corresponds to a more complex TADF model, including three excited states (Fig. S35). This system of equations also has analytical solution, although it is very cumbersome. Moreover, even the simplified version of this solution, realized in the case of fast establishment of equilibrium between three excited states, contains too many parameters (two energy differences, $\Delta E_{S_1-T_1}$ and $\Delta E_{T_2-T_1}$, and three rate constants). Therefore, we first calculated a series of $\tau(T)$ dependences using a four-level model with typical parameter values, and then analyzed the entire calculated curve and its low- and high-temperature regions using a three-level model [equation (5)].

As an example, Figure S36 shows the theoretical curve obtained for the four-level system with the parameters, presented in the caption. As expected, the approximation of the curve in the low-temperature region gave the correct $k_{T1\to S0}$ value (10^2 s^{-1}); in turn, the ΔE_{ST} value (534 cm^{-1}) was severely underestimated and close to ΔE_{T2-T1}, the $k_{S1\to S0}$ value is unreasonably small (3.8×10^3 s^{-1}). The approximation over the entire temperature range gave the value $k_{T1\to S0}=$ 1.1×10^2 s^{-1}, close to the model parameter, however, the $k_{S1\to S0}$ (10^6 s^{-1}) was underestimated by two orders of magnitude, and the value of ΔE_{ST} (1600 cm^{-1}) was close to $\Delta E_{S_1-T_2}$. Finally, the approximation in the high-temperature region (200 – 300 K) with two variable parameters leads to $k_{S1\to S0} = 6.4\times10^7$ s^{-1}, which is only a third less than the model parameter, and $\Delta E_{ST}= 1900$ cm^{-1} is close to the model value for ΔE_{S1-T1}. Thus, even when four levels are involved, we can use a three-level model and determine one parameter from the low-temperature range (77 – ~110 K), and the other two from the high-temperature range (~200 – 300 K).
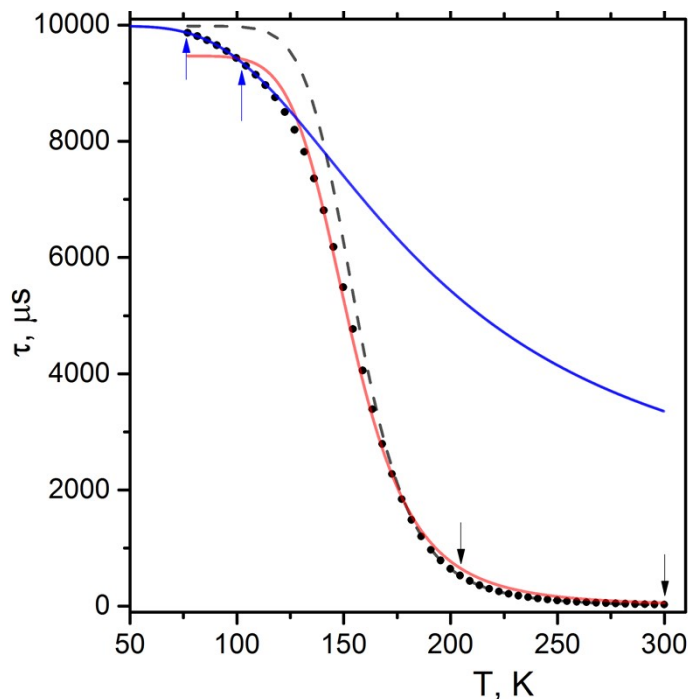
Figure S36. Calculated using four-level model temperature dependence of τ_{TADF} (black circles, $\Delta E_{S_1 - T_1} = 2000$ cm^{-1}, $\Delta E_{S_1 - T_2} = 1500$ cm^{-1} ($\Delta E_{T2 - T1} = 500$ cm^{-1}), $k_{T1 \to S0} = 10^2$ s^{-1}, $k_{S1 \to S0} = 10^8$ s^{-1}, $k_{S1 \to T1} = k_{S1 \to T2} = k_{T2 \to T1} = 10^{12}$ s^{-1}), its approximations using the three-level model in the temperature range 77 – 300 K (red curve), 77 – 104 K (blue curve) and ~200 – 300 K (black dashed curve).

Using the procedure described above, we have analyzed the experimental τ(T) dependences for complexes **3**–**5**, for which an unsatisfactory approximation is observed over the entire temperature range (77–300 K). Figure S37 shows that in the case of **3**, the individual fits in the low and high temperature ranges are almost identical to the fit over the entire range (black line), although the parameters of the best fit are significantly different (Table S8): the rate constant $k_{S1 \to S0}$ increases by a factor of 5, and the $\Delta E_{S1 - T1}$ by a third. In the case of complexes **4** and **5**, the individual fits deviate substantially from the fit over the entire range, with values of $k_{S1 \to S0}$ increasing by more than an order of magnitude and $\Delta E_{S1 - T1}$ by more than 50%.

We, understand that the situation can be much more complicated, and not only the participation of additional triplet states in the TADF process can cause the deviation of the temperature dependence of the PL time from that described by the standard three-level model. However, the presence of additional triplet states is not just an assumption, but a fact based on our TD-DFT calculations.

Analysis of the data in Table S8 shows that fitting over the entire temperature range leads to significantly different values of $k_{S1 \to S0}$, which decrease by more an order of magnitude from complex **1** to **5**, while the high temperature fitting gave close values of $k_{S1 \to S0}$ and $\Delta E_{S1 - T1}$ for all complexes, which is more reasonable given the similar electronic nature of the excited states of **1** to **5**. As expected, the relativistic nature of Au significantly affects the rate constant of the intersystem crossing ($k_{T1 \to S0}$), but there is no reason for it to affect $k_{S1 \to S0}$.

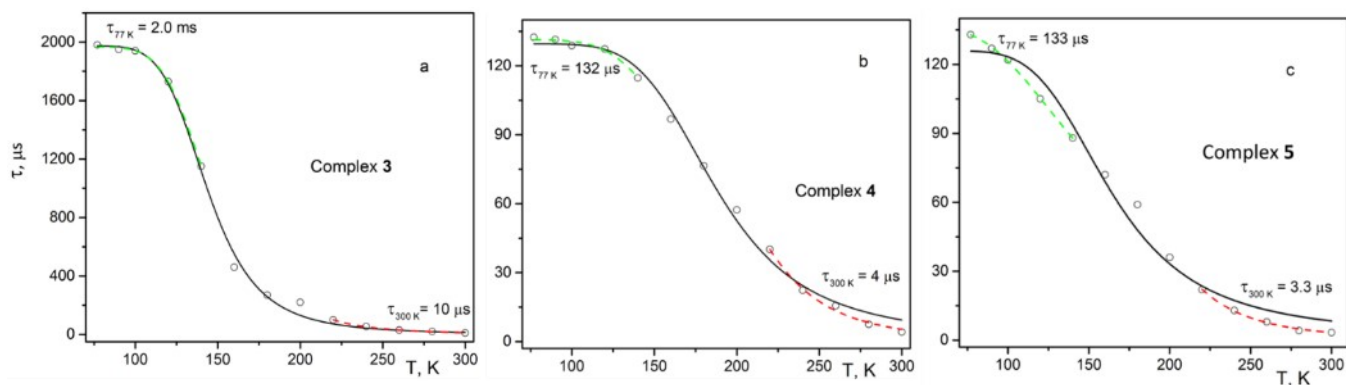**Figure S37.** Experimental temperature dependences of photoluminescence time (τ) for complexes **3**–**5** (open black circles) and their best fits using equation (5) in the entire temperature range (solid black lines), in the low-temperature (green dashed lines) and high-temperature (red dashed lines) ranges (best-fit parameters are given in Table S6).

Table S8. The best-fit parameters of the three-level model obtained by fitting over the entire temperature range (as in Table S5), and those obtained for **3**–**5** by fitting in the low-temperature and high-temperature ranges.

N	77 – 300 K				77 – 120 K	220 – 300 K		
	$k_{T1 \to S0}$	$k_{S1 \to S0}$	ΔE_{S1-T1}	K(298 K)	$k_{T1 \to S0}$	$k_{S1 \to S0}$	ΔE_{S1-T1}	K(298 K)
1	$(5.88\pm0.02)\times10^2$	$(1.6\pm0.3)\times10^8$	900 ± 10	232 ± 11	–	–	–	–
2	$(3.38\pm0.02)\times10^2$	$(1.3\pm0.5)\times10^8$	1230 ± 40	1140 ± 240	–	–	–	–
3	$(5.06\pm0.07)\times10^2$	$(1.9\pm1.1)\times10^7$	940 ± 60	280 ± 90	$(5.08\pm0.02)\times10^2$	$(0.9\pm0.2)\cdot10^8$	1230 ± 40	1140 ± 240
4	$(7.7\pm0.1)\times10^3$	$(2.3\pm0.9)\times10^7$	900 ± 60	230 ± 80	$(7.61\pm0.06)\times10^3$	$(3.4\pm1.9)\cdot10^8$	1340 ± 90	1900 ± 1100
5	$(7.9\pm0.2)\times10^3$	$(8.8\pm5.2)\times10^6$	680 ± 70	80 ± 30	$(7.34\pm0.06)\times10^3$	$(2.5\pm0.8)\cdot10^8$	1180 ± 50	890 ± 240

In principle, parameters of the three-level model, namely, $k_{T1 \to S0} = k_{rad}^T + k_{nr}^T$ and $k_{S1 \to S0} = k_{rad} + k_{nr}$, can also be temperature dependent. In our opinion, the radiation rate constant (k_{rad}) should not change with temperature, since in the crystalline state the geometry of our complexes also does not undergo changes with temperature. However, the transition from the crystal to the solution can cause quite significant changes in geometry, as found from calculations for complexes **4** and **5**. As for k_{nr}, in solution it can grow significantly with increasing temperature due to bimolecular quenching processes, but in the solid state, such processes are absent. In the late 60s, much attention was paid to both experimental and theoretical studies of photophysical processes, including non-radiative relaxation of excited states.[37] It was found that in some cases a small increase of k_{nr} (2–3 times in the range 77–300 K) is observed for aromatic molecules immobilized in polymer films. Moreover, the high quantum yield of TADF (about 90%) for **3** and **4** indicates an insignificant contribution of the k_{nr} to the overall rate constant ($k_{rad} + k_{nr}$). So, most likely, the parameters of the three-level model are independent of temperature, at least for **3** and **4**, and for **5** such a dependence should be weak.

§11. References

[1]   H. C. E. McFarlane, W. McFarlane, *Polyhedron*, 1988, **7**, 1875.
[2]   V. Jurkauskas, J. P. Sadighi, S. L. Buchwald, *Org. Lett.*, 2003, **5**, 2417.
[3]   L. Hintermann, *Beilstein J. Org. Chem.*, 2007, **3**, 22.
[4]   P. de Frémont, N. M. Scott, E. D. Stevens, T. Ramnial, O. C. Lightbody, C. L. B. Macdonald, J. A. C. Clyburne, C. D. Abernethy, S. P. Nolan, *Organometallics*, 2005, **24**, 6301.
[5]   P. de Frémont, N. M. Scott, E. D. Stevens and S. P. Nolan, *Organometallics*, 2005, **24**, 2411.

[6] P. Kubelka, *J. Opt. Soc. Am.* **1948**, *38*, 448–457.

[7] *CrysAlisPro ver. 1.171.38.46, Rigaku Oxford Diffraction,* **2015**.

[8] *APEX2, APEX3, SAINT, SADABS. Bruker Advanced X-ray Solutions; Bruker AXS Inc., Madison, WI,* **2017**

[9] G. M. Sheldrick, *Acta Crystallogr. A* 2015, **71**, 3.

[10] G. M. Sheldrick, *Acta Crystallogr. C* 2015, **71**, 3.

[11] (a) *The Quantum Theory of Atoms in Molecules* (Eds.: C. F. Mottaand, R. J. Boid), Wiley-VCH, Weinheim, 2007; (b) R. F. W. Bader, *Monatsh. Chem.* 2005, **136**, 819–854; c) R. F. W. Bader, *Atoms in Molecules: A Quantum Theory*, Oxford University Press, Oxford, 1990.

[12] (a) A. E. Reed, L. A. Curtiss, F. Weinhold, *Chem. Rev.* 1988, **88**, 899–926; (b) F. Weinhold, C. R. Landis, *Valency and Bonding: A Natural Bond Orbital Donor-Acceptor Perspective*; Cambridge University Press: Cambridge, U.K.

[13] T. Lu, F. Chen, *J. Comput. Chem*. **2012**, *33*, 580–592.

[14] B. A. Hess, *Phys. Rev. A* 1986, **33**, 3742–3748.

[15] (a) A. D. Becke, *J. Chem. Phys*. 1993, **98**, 5648–5652; (b) C. Lee, W. Yang, R. G. Parr, *Phys. Rev. B* 1988, **37**, 785–789.

[16] S. Huzinaga, M. Klobukowski, *Chem. Phys. Lett*. 1993, **212**, 260–264.

[17] D. A. Pantazis, X. Y. Chen, C. R. Landis, F. Neese, *J. Chem. Theory Comput*. 2008, **4**, 908–919.

[18] E. D. Glendening, C. R. Landis, F. Weinhold, *J. Comput. Chem.* 2019, **40**, 2234–2241.

[19] *Gaussian 16, Revision C.01*, M. J. Frisch, G. W. Trucks, H. B. Schlegel, G. E. Scuseria, M. A. Robb, et al., Gaussian, Inc., Wallingford CT, 2019.

[20] A. Dreuw, M. Head-Gordon, Chem. Rev. 2005, 105, 4009–4037.

[21] F. Weigend, R. Ahlrichs.*Phys. Chem. Chem. Phys*. 2005, **7**, 3297–3305.

[22] D. J. Rowe, *Rev. Mod. Phys.* 1968, **40**, 153–166.

[23] B. de Souza, G. Farias, F. Neese, R. Izsak, *J. Chem. Theory Comput.* 2019, 15, 1896–1904.

[24] M. Roemelt, D. Maganas, S. DeBeer, F. Neese, *J. Chem. Phys.* **2013**, *138*, 204101.

[25] (a) S. Grimme, *J. Comput. Chem*. 2006, **27**, 1787–1799, (b) S. Grimme, J. Antony, S. Ehrlich, H. Krieg, *J. Chem. Phys.* 2010, **132**, 154104.

[26] V. Barone, M. Cossi, *J. Phys. Chem. A* 1998, **102**, 1995–2000.

[27] (a) F. Neese, F. Software update: the ORCA Program System, version 4.0. *Wiley Interdiscip. Rev. Comput. Mol. Sci*. 2018, **8**, e1327; (b) F. Neese, Software Update: The ORCA Program System—Version 5.0. *Wiley Interdiscip. Rev. Comput. Mol. Sci.* 2022, **12**, e1606.

[28] G. A. Andrienko, Chemcraft – Graphical Software for Visualization of Quantum Chemistry Computations. See https//www. chemcraftprog.com.

[29] a) E. Espinosa, I. Alkorta, J. Elguero, E. Molins, From weak to strong interactions: A comprehensive analysis of the topological and energetic properties of the electron density distribution involving X–H…F–Y systems, *J. Chem. Phys*. 2002, **117**, 5529-5542; b) D. Marabello, R. Bianchi, G. Gervasio, F. Cargnoni, An experimental (120 K) and theoretical electron-density study of $KMnO_4$ and $KClO_4$, *Acta Crystallogr. A*. 2004, **60**, 494-501.

[30] B. Cordero, V. Gromez, A. E. Platero-Prats, M. Revres, J. Echeverrıa, E. Cremades, F. Barragran, S. Alvarez, *Dalton Trans*., **2008**, 2832–2838.

[31] P. Pyykko, Theoretical chemistry of gold, *Angew. Chem. Int. Ed*., 2004, **43**, 4412–4456.

[32] S. Alvarez, *Dalton Trans*., 2013, **42**, 8617–8636.

[33] A. Schinabeck, J. Chen, L. Kang, T. Teng, H. H. H. Homeier, A. F. Suleymanova, M. Z. Shafikov, R. Yu, C.-Z. Lu, H. Yersin, *Chem. Mater*. 2019, **31**, 4392−4404.

[34] A. S. Davydov, *Sov. Phys. Usp*., 1964, **7**, 145−178.

[35] T. R. Gosnell, *Fundamentals of Spectroscopy and Laser Physics*, Cambridge University Press, Cambridge, 2002.

[36] H. Yersin, R. Czerwieniec, M. Z. Shafikov, A. F. Suleymanova, TADF Material Design: Photophysical Background and Case Studies Focusing on Cu(I) and Ag(I) Complexes, in *Highly Efficient OLEDs: Materials Based on Thermally Activated Delayed Fluorescence,* Ed. H. Yersin, 2019, pp. 1–60, Wiley-VCH Verlag GmbH & Co.

[37] J. B. Birks, Photophysics of Aromatic Molecules. Wiley Inter-Science, London 1970.